RSC Advances

ROYAL SOCIETY OF CHEMISTRY

PAPER

View Article Online
View Journal | View Issue

Check for updates

Cite this: *RSC Adv.*, 2026, **16**, 23895

Engineering a CeO_2–ZnO nanocomposite on biochar for synergistic adsorption-photocatalysis and enhanced multipollutant wastewater remediation

Mahmoud F. Mubarak,[a] Elbadawy A. Kamoun,*[b] M. Y. Nassar[b] and Tahany Mahmoud*[a]

Received 11th January 2026
Accepted 20th April 2026

DOI: 10.1039/d6ra00287k

rsc.li/rsc-advances

This study presents a novel CeO_2–ZnO/biochar (CeZB) ternary composite, synthesized *via* a straightforward hydrothermal method, and investigates its dual functionality in the adsorptive removal and photocatalytic degradation of multiple wastewater pollutants. Structural and morphological analyses confirmed the successful incorporation of CeO_2 and ZnO nanoparticles onto the biochar support, which enhanced the surface area and availability of active sites. The resulting composite exhibited a high specific surface area of 215.3 $m^2\ g^{-1}$ and a bandgap energy of 2.48 eV, making it capable of visible-light-driven photocatalysis. Within 60 minutes, the CeZB composite showed good adsorption capability for methylene blue (MB, 198.6 mg g^{-1}) and tetracycline (TC, 163.2 mg g^{-1}) at pH 7. Under simulated solar irradiation, photocatalytic degradation efficiencies reached 96.5% for MB and 91.3% for TC within 90 minutes. Enhanced charge separation, reactive oxygen species (ROS) production, and π–π interactions enabled by the biochar matrix were identified as the synergistic mechanism. Kinetic and equilibrium analyses indicated that the adsorption process is governed by monolayer chemisorption, as evidenced by its strong conformity to the Langmuir isotherm model and the pseudo-second-order kinetic model, with correlation coefficients exceeding 0.99. The rate constants for the photocatalytic degradation were 0.031 min^{-1} for MB and 0.027 min^{-1} for TC, indicating pseudo-first-order kinetics. The composite's stability was confirmed by reusability tests conducted over five cycles, which revealed a minor reduction in performance (<6%). All things considered, the CeZB ternary composite offers a viable and sustainable method for using combined adsorption-photocatalysis to treat complex wastewater that contains both dyes and antibiotics.

1 Introduction

Continuous discharge from industrial, agricultural, and pharmaceutical sources has led to the accumulation of pollutants such as synthetic dyes and antibiotics in aquatic ecosystems. These contaminants pose serious environmental and health risks due to their toxicity, persistence, and resistance to conventional biological treatment. Among the most common wastewater pollutants are methylene blue (MB), a cationic dye used extensively in textile and leather industries, and tetracycline (TC), a widely employed broad-spectrum antibiotic.[1–4] When they coexist in water bodies, the ecological effects are increased, resulting in the growth of bacteria resistant to antibiotics and disturbance of aquatic life. Trace-level organic micropollutants are frequently difficult to remove using conventional wastewater treatment techniques like coagulation, membrane filtration, and activated sludge systems. As a result, the demand for sustainable and integrated methods that can effectively remove several types of pollutants is growing.[5–7]

Among the broad landscape of semiconductor-based photocatalytic materials, zinc oxide (ZnO) and cerium oxide (CeO_2) have carved out a prominent position driven by a convergence of exceptional attributes including pronounced oxidative capacity under both ultraviolet and visible irradiation, robust resistance to photochemical degradation, and distinctive redox-active behavior. ZnO has a suitable bandgap and strong photocatalytic activity, while CeO_2 has a good oxygen storage capacity and can help separate photogenerated charge carriers.[8–11] By increasing surface dispersion, improving adsorption capacity, and promoting interfacial electron transfer, these oxides can be successfully incorporated into carbonaceous supports like biochar to get around these restrictions.[11–13]

---

[a] Petroleum Application Department, Egyptian Petroleum Research Institute (EPRI), Cairo 11727, Egypt. E-mail: tahany.mahmoud.a@gmail.com

[b] Department of Chemistry, College of Science, King Faisal University, Al-Ahsa 31982, Saudi Arabia. E-mail: ekamoun@kfu.edu.sa; badawykamoun@yahoo.com

Produced through the high-temperature thermochemical conversion of biomass, biochar is a carbon-rich material distinguished by its highly porous architecture, rich surface functional groups, and environmentally sustainable nature. Beyond its strong capacity for pollutant adsorption, it also functions as an efficient supporting matrix that enhances the photocatalytic activity of metal oxides *via* synergistic interactions between the components.[14–17] Thus, a promising approach to treating multi-pollutant systems in wastewater is the development of ternary composites that combine CeO_2, ZnO, and biochar.[18] Recent research has emphasized the development of *Z*-scheme architectures along with the integration of conductive carbon-based matrices as effective strategies to promote interfacial charge transfer while minimizing electron–hole recombination. Advanced materials such as defect-engineered metal oxides, hybrid semiconductor systems, and carbon-supported nanostructures have shown remarkable potential for environmental remediation applications under visible light irradiation. These developments provide a strong foundation for designing multifunctional composites with synergistic adsorption-photocatalysis capabilities, as explored in the present study.[19–24]

This study aims to synthesize and characterize a CeO_2–ZnO/biochar ternary composite and evaluate its performance in the simultaneous adsorption and photocatalytic degradation from aqueous solutions under visible light irradiation. Despite the extensive research on individual ZnO, CeO_2, and their binary composites, several critical limitations remain unresolved, including rapid charge recombination, limited adsorption capacity, and insufficient performance in treating complex multipollutant systems. Previous research has primarily addressed adsorption and photocatalysis as separate processes, with few attempts to combine both functionalities within a single material platform. Moreover, the interfacial interaction between CeO_2 and ZnO in supported systems has not been adequately explored, particularly in terms of charge transfer pathways and synergistic mechanisms.

Within this context, the current study presents a novel CeO_2–ZnO/biochar (CeZB) ternary composite, wherein biochar acts as both a high-surface-area support and an electron mediator, thereby enhancing interfacial charge transfer. The uniqueness of this work lies in: (i) the rational design of a ternary heterostructure enabling simultaneous adsorption and visible-light-driven photocatalysis, (ii) the enhanced multipollutant removal capability targeting both dye (MB) and antibiotic (TC) contaminants, and (iii) the improved charge separation efficiency arising from the synergistic interaction between CeO_2, ZnO, and the conductive biochar matrix. This integrated approach distinguishes the present work from previously reported systems and provides a scalable and efficient strategy for advanced wastewater treatment applications.

2 Methodology

2.1 Materials

The primary metal precursors employed for synthesis of CeO_2 and ZnO nanoparticles were cerium(III) nitrate hexahydrate ($Ce(NO_3)_3\cdot 6H_2O$, 99.5% purity) as well as zinc nitrate hexahydrate ($Zn(NO_3)_2\cdot 6H_2O$, 99% purity), respectively, both obtained from Sigma-Aldrich (USA). Sodium hydroxide (NaOH, 98% purity) as well as ethanol (C_2H_5OH, 99.9% purity) were provided by Sigma-Aldrich and used directly without any additional purification steps. Methylene blue (MB, dye content ≥82%) and tetracycline hydrochloride (TC, ≥95% purity) were supplied by Merck (Germany). Raw biomass in the form of rice husk was sourced from a local agricultural processing facility in Punjab, India, and used for biochar preparation. All experimental procedures were performed using deionized water with a resistivity of 18.2 MΩ cm, produced by a Millipore water purification system.

2.2 Synthesis of biochar

For this study, the authors used biochar made from rice husk biomass, mainly because it's rich in lignocellulosic materials and easy to get hold of. Prior to pyrolysis, the biomass was thoroughly washed, dried at 105 °C for 24 hours, and ground into a fine powder. The pyrolysis process was subsequently performed in a muffle furnace under limited oxygen at 500 °C for two hours. That temperature is known to help form aromatic carbon structures and boost graphitic areas in the biochar both of which are important for creating strong communications with aromatic pollutants.

At 500 °C, the biochar ends up partially carbonized, giving it: key features of the biochar included a high surface area, an abundance of oxygen-containing functional groups (–OH, –COOH) and well-developed conjugated π-electron systems. All these features work together to improve adsorption. Plus, when this biochar was combined with semiconductor oxides, it also helps shuttle electrons around during photocatalysis.

2.3 Synthesis of CeO_2–ZnO/biochar ternary composite

A one-pot hydrothermal method was employed to prepare the CeO_2–ZnO/biochar composite. In a representative synthesis, 0.01 mol each of $Ce(NO_3)_3\cdot 6H_2O$ and $Zn(NO_3)_2\cdot 6H_2O$ were dissolved in 100 mL of deionized water under continuous magnetic stirring until a homogeneous solution formed. At the same time, we placed 1 gram of biochar in 50 mL of ethanol, then subjected it to ultrasonication for half an hour to ensure it was well-dispersed and homogeneous. We then began gradually adding the metal nitrate solution to the suspension while stirring for one hour. Finally, we added a 1 M sodium hydroxide solution drop by drop until the pH reached approximately 10, which facilitated the formation and precipitation of metal hydroxides.

A Teflon-lined autoclave (200 mL capacity) served as the reaction vessel into which the prepared suspension was carefully loaded prior to solvothermal processing. Temperature was maintained at 180 °C across a 12-hour holding period, after which the system was left undisturbed until it reached ambient temperature through passive cooling. Centrifugal separation was then employed to isolate the solid precipitate, which underwent a sequential purification protocol alternating between ethanol and deionized water rinses across three successive cycles per solvent. Moisture elimination was

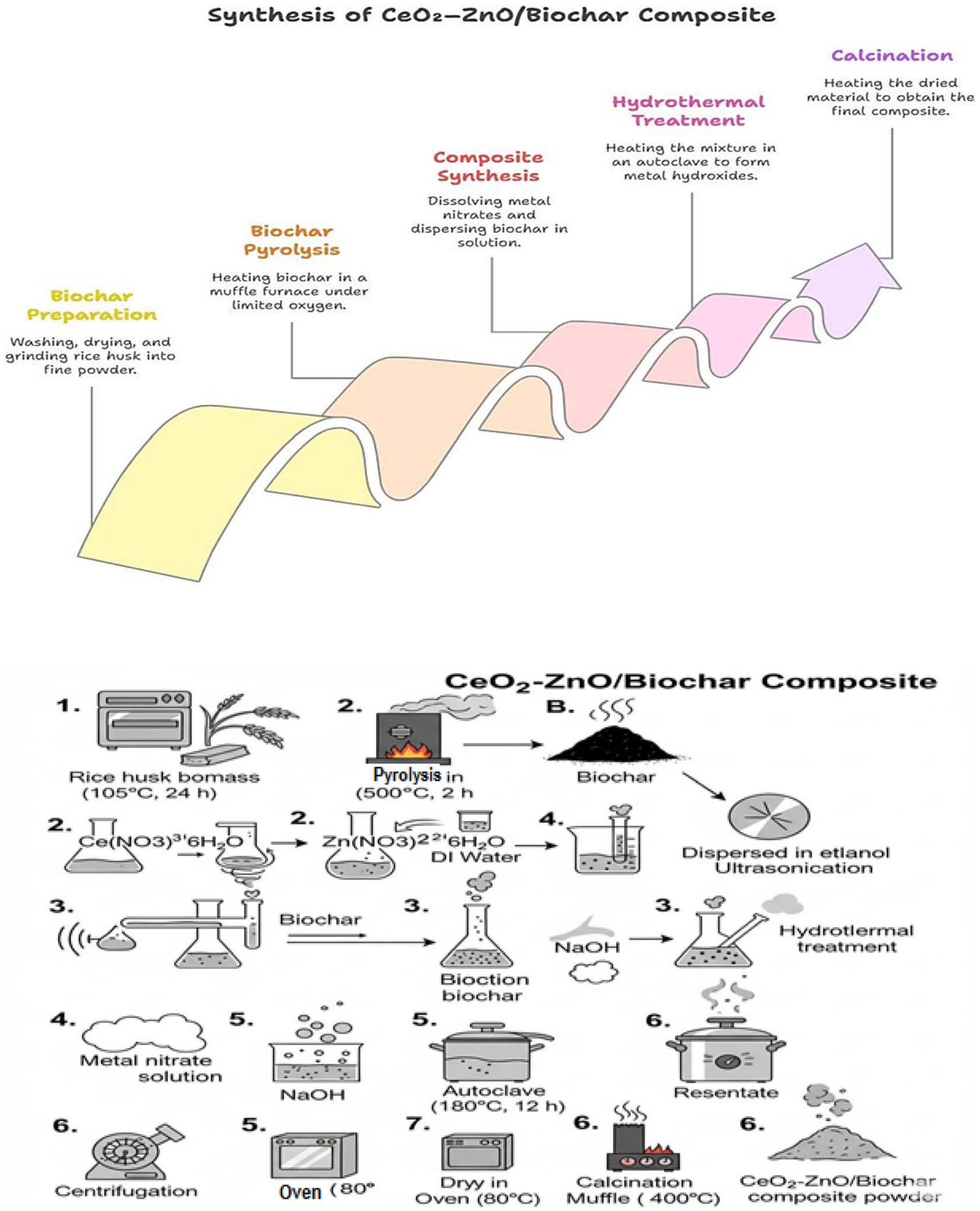

Fig. 1 Scheme of synthesis of CeO_2–ZnO/biochar composite.

accomplished by placing the recovered solid in a vacuum oven operating at 80 °C throughout an overnight drying period. Thermal post-treatment followed, wherein the dried powder was introduced into a muffle furnace and held at 400 °C for two hours, a calcination step that promoted the emergence of well-ordered crystalline domains within the CeO_2–ZnO/biochar composite architecture. The complete synthetic pathway is visually summarized in Fig. 1.

2.4 Characterization

To establish the crystallographic identity of each synthesized material, diffraction patterns were acquired using a Bruker D8 Advance diffractometer, wherein Cu Kα radiation ($\lambda = 1.5406$ Å) functioned as the primary excitation source at a voltage–current configuration of 40 kV and 30 mA. A dual-mode electron microscopy approach was subsequently adopted to interrogate both topographical features and chemical constituency – a JEOL JSM-7610F field-emission instrument, operating in conjunction with energy-dispersive X-ray spectroscopy, delivered spatially resolved elemental mapping alongside high-fidelity surface imaging. Where finer structural detail was demanded, nanometer-level resolution was unlocked through transmission electron microscopy in its high-resolution mode (HRTEM), executed on a JEOL JEM-2100 platform running at a 200 kV accelerating potential. A Micromeritics ASAP 2020 analyzer facilitated the acquisition of nitrogen adsorption–desorption profiles at 77 K, from which the Brunauer–Emmett–Teller framework was applied to extract a comprehensive textural portrait of each material, spanning surface area magnitude, cumulative pore volume, and prevailing pore dimensions. Shifting attention to optical behavior, a Shimadzu UV-2600 spectrometer operating in diffuse reflectance mode (UV-vis DRS) was recruited to map how each sample interacted with incident radiation across the ultraviolet and visible spectral windows, yielding insight into electronic band transitions. Rounding out the physicochemical characterization suite, chemically distinct surface functionalities were fingerprinted through Fourier-transform infrared spectroscopy, with spectral data collected on a Thermo Nicolet iS10 platform across the diagnostically informative infrared region.

2.5 Batch adsorption measurement

Batch experimentation served as the methodological backbone for evaluating how effectively the CeO_2–ZnO/biochar composite stripped methylene blue (MB) and tetracycline (TC) from aqueous matrices. Working solutions spanning an initial concentration window of 10 to 100 mg L^{-1} were freshly prepared in 100 mL volumes prior to each trial. Medium acidity was systematically varied across the pH 3–10 interval, with dropwise addition of either 0.1 M HCl or 0.1 M NaOH serving as the adjustment vehicle. Into each reaction vessel, a precisely weighed 20 mg portion of the composite adsorbent was introduced, whereupon the resulting mixture was subjected to continuous orbital agitation at 150 rpm under a thermostated environment of 25 ± 1 °C contact durations ranging from 10 to 180 minutes were explored to build a comprehensive picture of temporal adsorption evolution.

Throughout the experimental timeline, small-volume liquid samples were periodically extracted from each reaction vessel, passed through 0.22 μm syringe filters to eliminate particulate interference, and subsequently directed toward spectrophotometric quantification – a UV-2600 instrument (Shimadzu, Japan) was employed, targeting the characteristic absorption maxima of MB and TC at 664 nm and 357 nm, respectively.[25,26] The extent of pollutant uptake was then numerically expressed through two complementary metrics: adsorption capacity (q_e, mg g^{-1}) and removal efficiency (%), both computed *via* the mathematical relationship presented in eqn (1).

$$q_e = \frac{(C_0 - C_e) \times V}{m}$$

$$\text{Removal efficiency}(\%) = \frac{(C_0 - C_e)}{C_0} \times 100. \tag{1}$$

In these equations, C_0 and C_e (mg L^{-1}) denote the initial and equilibrium concentrations, respectively, V represents the solution volume (L), and m is the mass of the adsorbent (g).

A four-model analytical architecture, spanning Langmuir and Freundlich isotherms at equilibrium and pseudo-first-order and pseudo-second-order equations across the kinetic dimension, was assembled around the experimental dataset to extract mechanistic clarity from observed adsorption behavior.[27,28]

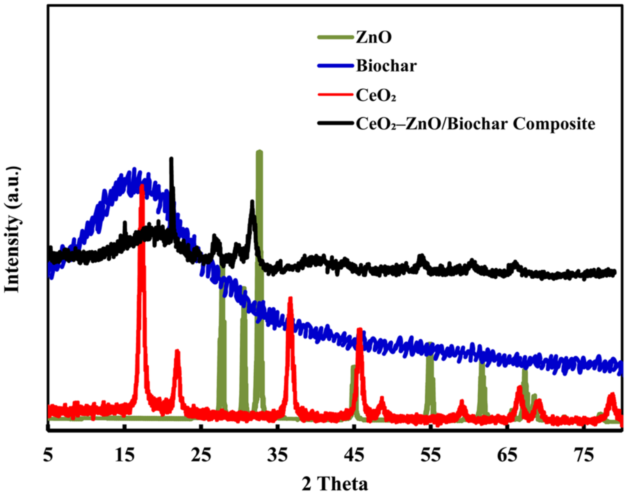

Fig. 2 This figure shows biochar, zinc oxide (ZnO), and cerium dioxide (CeO_2) the X-ray diffraction (XRD), patterns as well as the CeO_2–ZnO composite loaded onto biochar.

2.6 Photocatalytic degradation

Visible light photocatalytic performance was benchmarked using a 300 W xenon arc lamp as the irradiation source, fitted with a UV cut-off filter ($\lambda > 420$ nm) to confine the delivered spectrum strictly to the visible region. Aqueous preparations of MB and TC, each calibrated to an initial pollutant loading of 20 mg L^{-1}, constituted the target matrices against which degradation efficiency was assessed. Each experimental run was assembled by dispersing 20 mg of the CeO_2–ZnO/biochar composite into 100 mL of the respective pollutant solution, housed within a 250 mL quartz reactor vessel. Prior to activating the light source, the resulting suspension underwent a 30 minute dark-conditioning phase under continuous magnetic

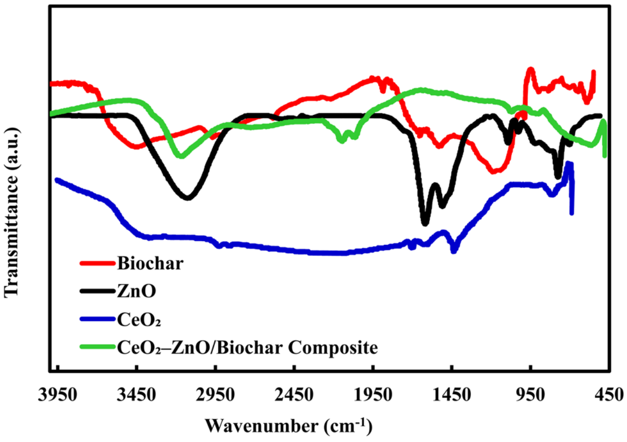

Fig. 3 This figure shows the FT-IR spectra of biochar, zinc oxide (ZnO), and cerium dioxide (CeO_2), as well as the CeO_2–ZnO composite loaded onto biochar.

agitation – a prerequisite step designed to drive the system toward adsorption–desorption equilibrium before any photochemical transformation was initiated.

At regular time intervals following illumination (15, 30, 45, 60, 75, and 90 min), aliquots of the suspension were collected, centrifuged at 5000 rpm for 10 minutes, and analyzed by UV-vis spectrophotometry for the determination of residual

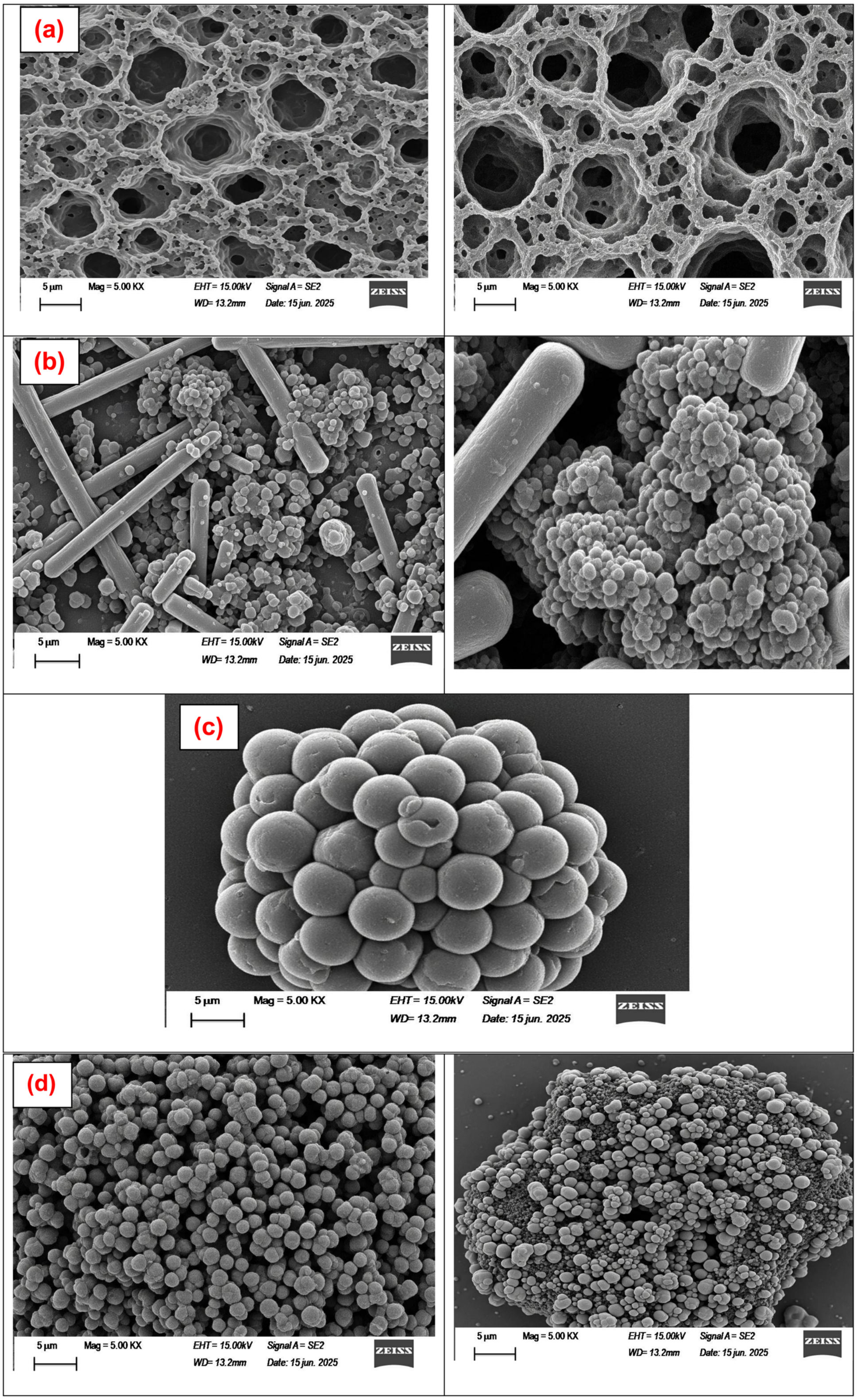

Fig. 4 FE-SEM Images of (a) biochar, (b) ZnO, (c)CeO_2 and (d) CeO_2–ZnO/biochar composite.

concentrations of the dye as well as antibiotic.[28] The following equation was used to calculate the photocatalytic degradation efficiency:

$$\text{Degradation efficiency}(\%) = \frac{(C_0 - C_t)}{C_0} \times 100. \quad (2)$$

where, C_t denotes the concentration of the pollutant (mg L^{-1}) at a given time t (min).

Before light exposure, the mixture was magnetically stirred in the dark for 60 minutes. This step was meant to let pollutant molecules reach adsorption–desorption balance with the catalyst surface. Time of 60 minutes was chosen, because our earlier adsorption kinetics experiments (see Section 3.2.1) showed that's about how long it took for the system to reach equilibrium basically, when the adsorption capacity (q_t) leveled off. Getting that balance right before shining light is important. It helps us tell apart what's just adsorption from what's actual photocatalytic breakdown. So, once we turn the light on, any drop in pollutant concentration can confidently be credited to photocatalysis, not just sticking to the surface.[18,26]

3 Results and discussion

3.1 Characterization of CeO_2–ZnO/biochar composite

3.1.1 XRD analysis. XRD results verified the crystalline nature of the synthesized materials. In Fig. 2, XRD patterns of CeO_2–ZnO/biochar composite exhibit well-defined diffraction peaks attributable to both CeO_2 and ZnO phases, confirming their successful integration within the composite structure. The reflections detected at $2\theta = 28.6°$, 33.1°, 47.5°, and 56.3° are correlated with (111), (200), (220), and (311) planes, respectively, which are characteristic of cubic fluorite CeO_2 and are in good agreement with JCPDS card No. 34-0394. Concurrently, the reflections at 31.7°, 34.4°, and 36.2° are characteristic of the (100), (002), and (101) planes of hexagonal wurtzite ZnO (JCPDS 36-1451).[18] The broad, less intense hump observed around 20°–25° in the composite is attributed to the amorphous nature of biochar. No impurity peaks were detected, suggesting high purity and successful formation of the ternary composite. Crystallite sizes estimated using Scherrer equation were approximately 12.4 nm for ZnO and 14.7 nm for CeO_2.[17,28]

3.1.2 FTIR spectroscopy analysis. A three-feature infrared fingerprinting profile, anchoring a broad hydroxyl stretching

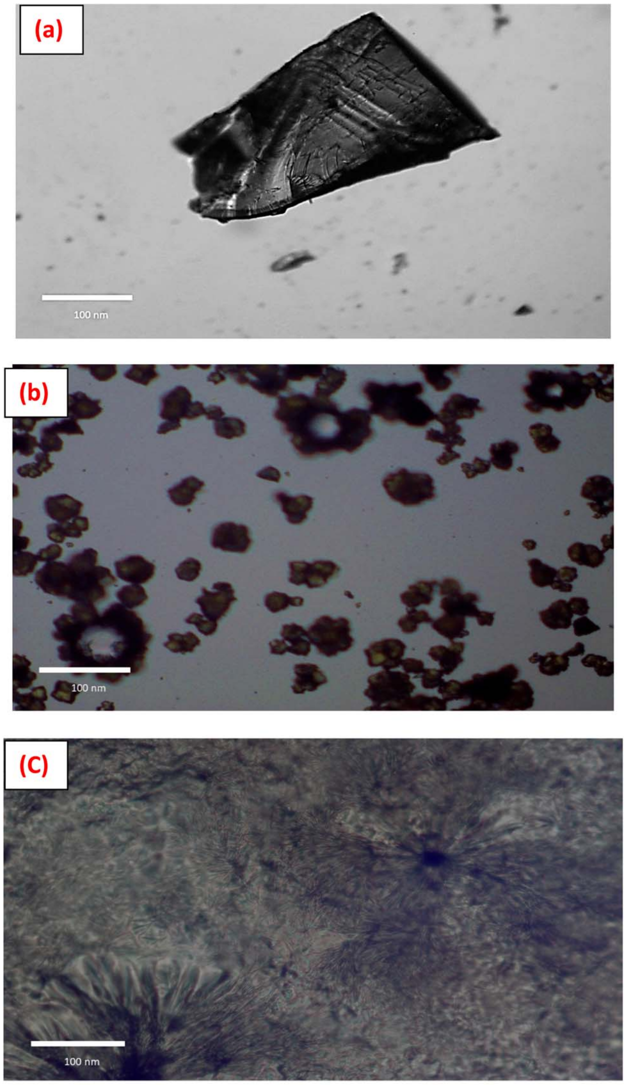

Fig. 5 TEM images of (a–c) CeO_2–ZnO/biochar composite showing dispersion of ZnO and CeO_2 nanoparticles on biochar matrix.

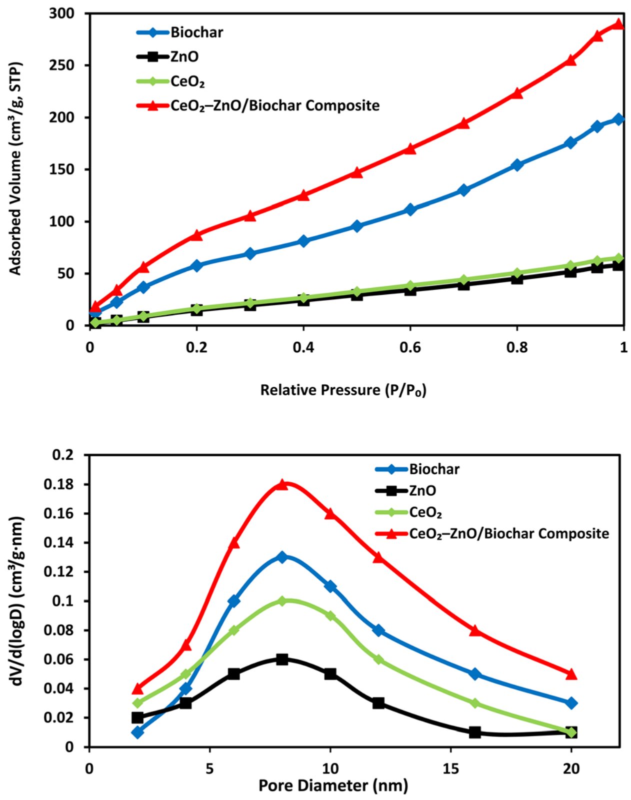

Fig. 6 N_2 adsorption–desorption isotherms (BET method) (up) and corresponding pore size distribution curves (BJH method) (down) for biochar, ZnO, CeO_2, and CeO_2–ZnO/biochar composite.

Table 1 BET results for biochar, ZnO, CeO_2, and CeO_2–ZnO/biochar composite

Sample	BET surface area ($m^2\ g^{-1}$)	Total pore volume ($cm^3\ g^{-1}$)	Average pore diameter (nm)
Biochar	153.7	0.31	7.8
ZnO	36.4	0.09	9.2
CeO_2	42.7	0.11	10.3
CeO_2–ZnO/biochar composite	215.3	0.42	8.1

signature at 3435 cm^{-1} across the surface functionalization domain, and resolving a carbonyl/carboxyl absorption band at 1630 cm^{-1} within the biochar-associated structural dimension, was extracted from FTIR spectra presented in Fig. 3, to decode the interfacial chemical architecture emerging from biochar–metal oxide integration within the composite framework. Furthermore, bands at 1385 and 1035 cm^{-1} associated with C–O bonds in phenolic and etheric groups are observed, confirming the organic nature of the matrix. In the low region (500–700 cm^{-1}), characteristic signals of Zn–O and Ce–O bonds appear, reflecting the formation of zinc and cerium oxides and their successful incorporation into the composite structure.

3.1.3 Surface morphology by (FE-SEM) investigation. Result of field emission scanning electron microscopy (FE-SEM), represented across Fig. 4a–d, confirmed a heterogeneous surface morphology in which CeO_2 and ZnO nanoparticles were uniformly distributed and firmly anchored throughout the porous biochar matrix. The biochar provided a large surface area and porous architecture, enabling effective distribution of the metal oxides. CeO_2 particles appeared as quasi-spherical clusters, while ZnO exhibited rod-like or granular morphology.[27]

3.1.4 HR-TEM investigation. HRTEM analysis further validated the nanostructured nature of the composite. ZnO and CeO_2 nanoparticles were clearly observed as discrete crystalline domains on the biochar surface (Fig. 5a and b). Distinct lattice fringes, corresponding to interplanar spacings of 0.31 nm and 0.28 nm, were unambiguously resolved from HRTEM analysis, confirming the presence of well-developed crystalline domains within the composite structure. These values correspond to the (111) crystal planes of cerium oxide (CeO_2) and the (100) crystal planes of zinc oxide (ZnO), respectively. The interfacial contact between the nanoparticles and the carbon support is also observed, indicating a strong interaction between them, which

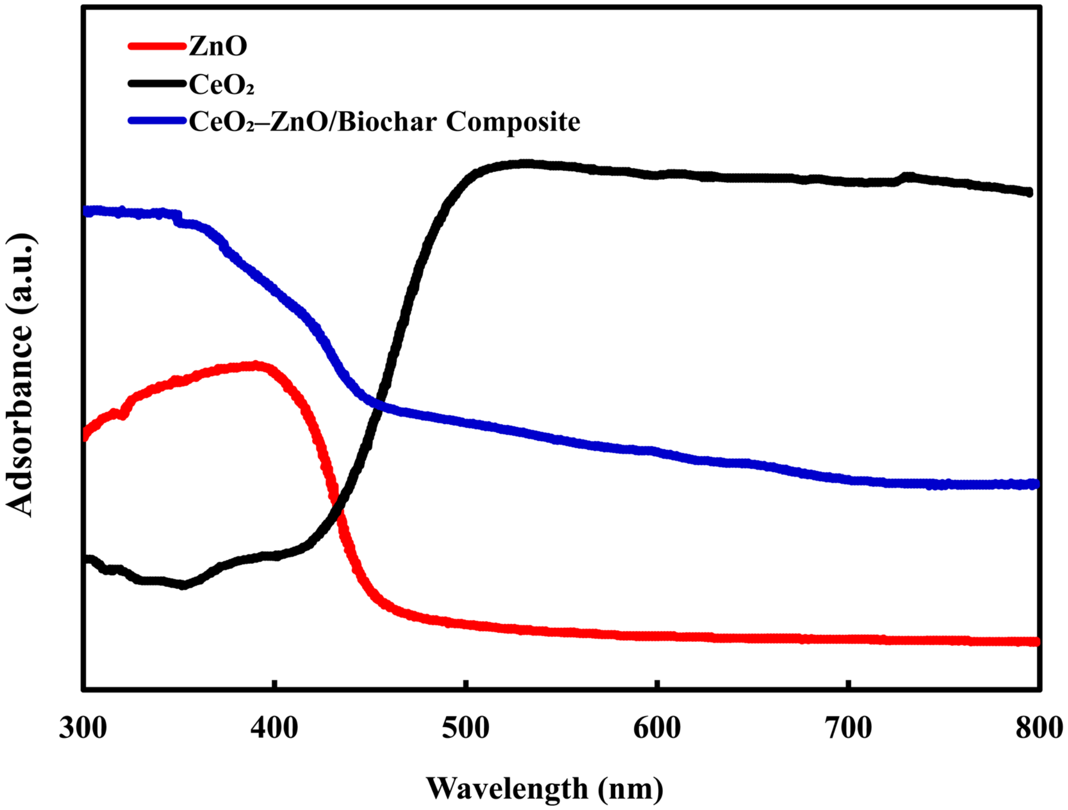

Fig. 7 UV-vis absorbance spectra of biochar, ZnO, CeO_2, and the CeO_2–ZnO/biochar composite.

contributes to improved charge separation and enhanced photocatalytic activity.[28]

3.1.5 BET surface area and porosity analysis. Fig. 6a presents N_2 BET isotherms of the composite, exhibiting characteristic type IV behavior with an H3-Type hysteresis loop (IUPAC classification), which confirms the mesoporous nature of materials. As summarized in Table 1, Brunauer–Emmett–Teller (BET) analysis revealed a high specific surface area of 215.3 $m^2\ g^{-1}$ for CeO_2–ZnO/biochar composite, significantly higher than pure CeO_2 (42.7 $m^2\ g^{-1}$) or ZnO (36.4 $m^2\ g^{-1}$), owing to the porous nature of biochar. The pore volume was 0.42 $cm^3\ g^{-1}$, and the average pore diameter is 8.1 nm, making

Table 2 Parameters derived from adsorption kinetic modeling

Pollutant	Model	Linear equation form	k (rate constant)	R^2	q_e, calc. (mg g^{-1})	q_e, exp. (mg g^{-1})
MB	Pseudo-first-order	$\log(q_e - q_t)$ *vs.* t	0.054 min^{-1}	0.961	182.4	198.6
MB	Pseudo-second-order	T/q_t *vs.* t	0.019 g mg^{-1} min^{-1}	0.995	196.1	198.6
TC	Pseudo-first-order	$\log(q_e - q_t)$ *vs.* t	0.048 min^{-1}	0.957	151.7	163.2
TC	Pseudo-second-order	T/q_t *vs.* t	0.016 g mg^{-1} min^{-1}	0.991	160.5	163.2

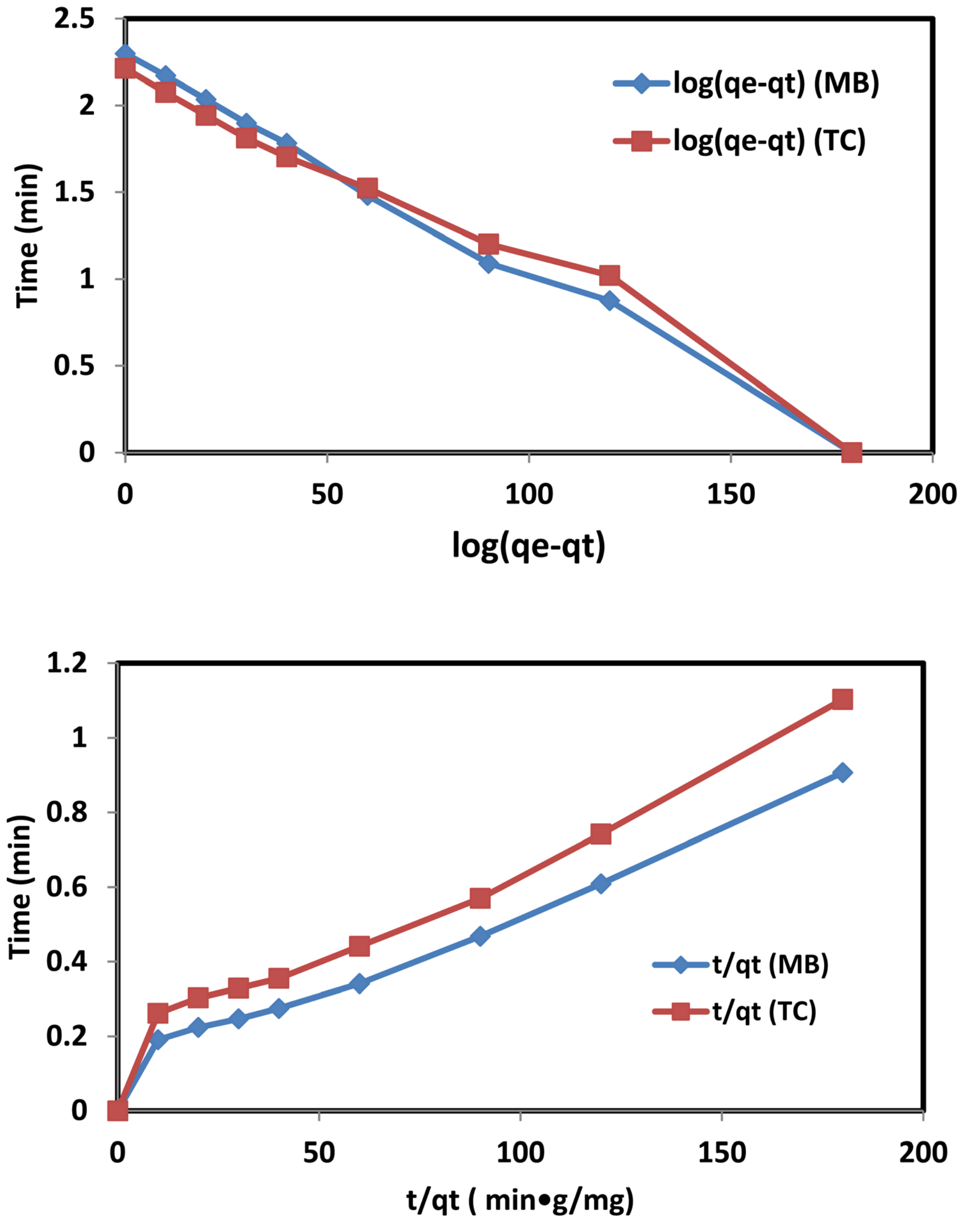

Fig. 8 Adsorption kinetics of CeO_2–ZnO/biochar composite toward tetracycline (TC) and methylene blue (MB); (up) represents a Pseudo-first-order model, while (down) represents a Pseudo-second-order model.

the composite suitable for adsorption and facilitating mass transport during photocatalysis.[29] Pore size distribution of CeO_2–ZnO/biochar composite, compared to pure components is shown in Table 1 and Fig. 6b.

3.1.6 Ultraviolet-visible diffuse reflectance spectroscopy (DRS). Optical properties were studied using UV-vis DRS and presented in (Fig. 7). The composite displayed strong absorption in the visible region (400–600 nm), significantly red-shifted compared to pure ZnO, indicating enhanced visible light

Table 3 Parameters derived from adsorption isotherm modeling

Pollutant	Model	Linear equation form	q_{max} (mg g^{-1})	K_L (L mg^{-1})	K_F [(mg g^{-1})(L mg^{-1})$^{1/n}$]	n	R^2
MB	Langmuir	C_e/q_e. *vs.* C_e	198.6	0.023	—	—	0.995
MB	Freundlich	$\log(q_e)$ *vs.* $\log(C_e)$	—	—	42.1	3.18	0.972
TC	Langmuir	C_e/q_e *vs.* C_e	163.2	0.018	—	—	0.992
TC	Freundlich	$\log(q_e)$ *vs.* $\log(C_e)$	—	—	36.8	2.97	0.965

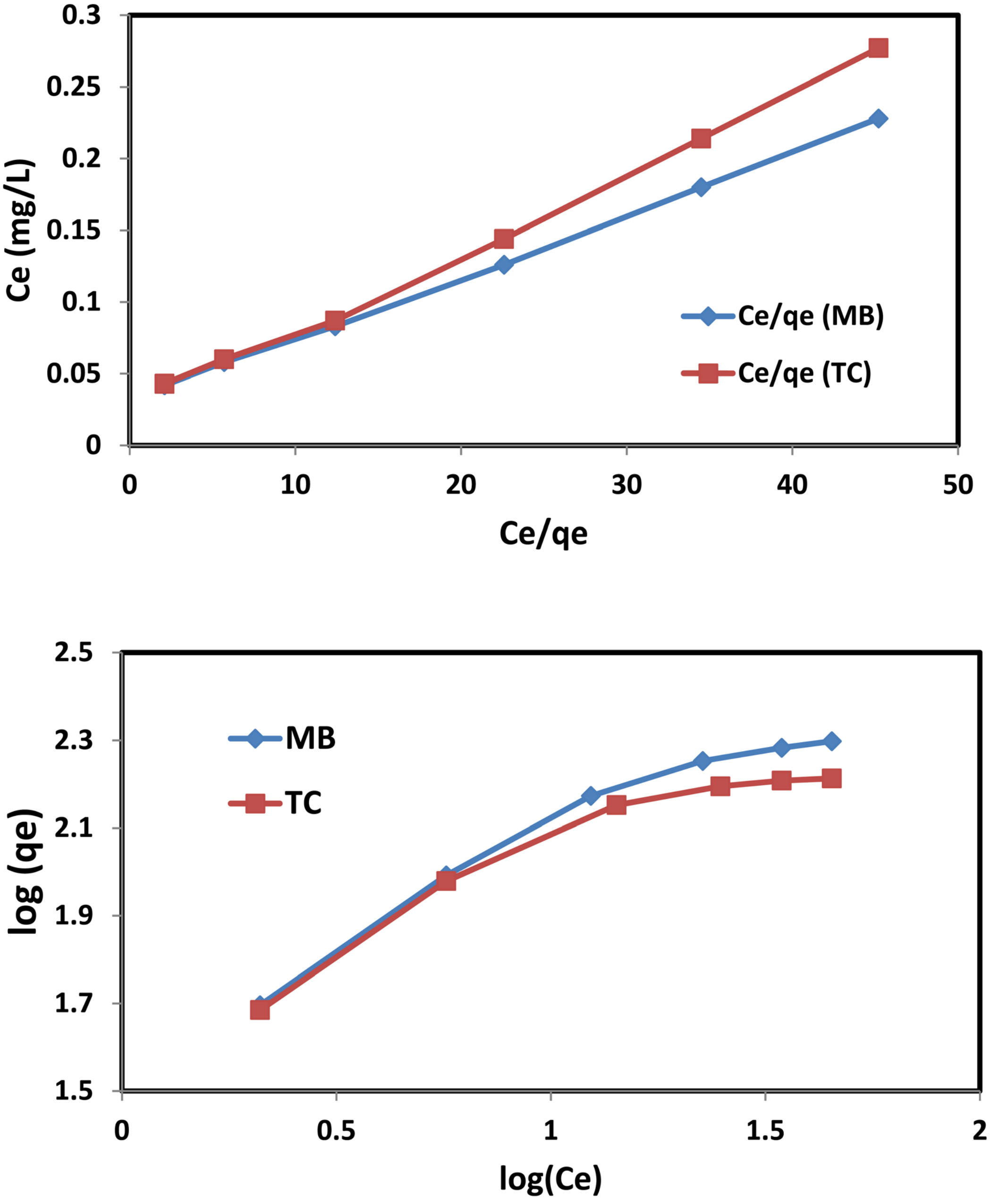

Fig. 9 Langmuir isotherm model plots (up) and Freundlich isotherm model plots (down) of CeO_2–ZnO/biochar composite for methylene blue (MB) and tetracycline (TC).

utilization. The bandgap energy was estimated using the Tauc plot and found to be 2.48 eV for the composite, lower than ZnO (3.21 eV) and CeO_2 (2.93 eV), suggesting synergistic bandgap narrowing due to the interaction between the components and improved light-harvesting capability.

Optical properties of the synthesized materials were systematically examined through UV-Vis diffuse reflectance spectroscopy (DRS), with the corresponding spectral profiles presented in Fig. 7a. CeO_2–ZnO/biochar composite really stands out it absorbs more visible light at 400–600 nm range than plain ZnO or CeO_2 do, which means it's better at capturing light.

Band gap determination for the synthesized material was carried out through Tauc-plot analysis, constructed from diffuse reflectance data processed *via* the Kubelka–Munk transformation. Assuming a direct allowed electronic transition, the optical band gap was extracted from the linear intercept of the $(\alpha h\nu)^2$ *versus* photon energy ($h\nu$) relationship, as presented in Fig. 7b. Extrapolation of the resulting linear segment toward the photon energy axis established an optical band gap of 2.48 eV for the ternary CeO_2–ZnO/biochar composite system. This value is markedly reduced relative to the characteristic band gaps of pristine ZnO (3.21 eV) and CeO_2 (2.93 eV), reflecting substantial electronic coupling among the constituent phases. Such a shift toward lower energy indicates enhanced absorption within the visible region, thereby improving the material's photoresponse under solar irradiation. The reduction in optical band gap observed across the ternary composite system is attributable to a concurrence of three mechanistically distinct contributing factors. Heterojunction formation at the CeO_2–ZnO interface induced charge redistribution and promoted electronic delocalization across the interfacial boundary. Concurrently, the introduction of oxygen vacancy states generated sub-bandgap energy levels within the electronic band structure, reducing the effective transition energy required for carrier excitation. Additionally, integration of the biochar framework into the composite architecture strengthened interfacial contact between constituent phases and improved electron mobility, collectively intensifying electronic coupling throughout the composite matrix.

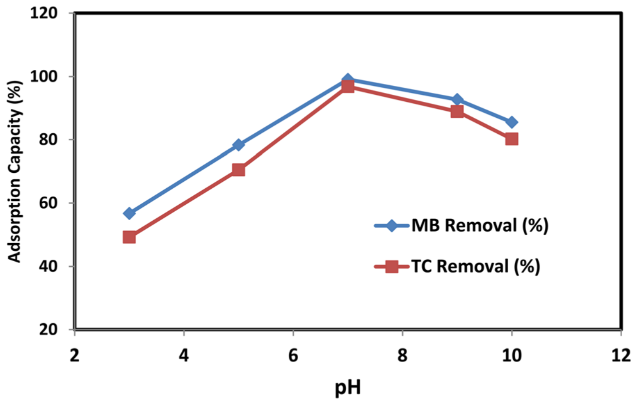

Fig. 10 Influence of solution pH on the adsorption capacity of MB and TC.

3.1.7 Band structure analysis using Mulliken electronegativity theory.

Valence band (VB) and conduction band (CB) edge potentials for both ZnO and CeO_2 were determined through the application of *Mulliken* electronegativity theory, as expressed in eqn (3):

$$\mathrm{ECB} = X - E_e - 0.5\,E_g,\quad \mathrm{EVB} = \mathrm{ECB} + E_g \tag{3}$$

where, X is absolute electronegativity, $E_e = 4.5$ eV is free electron energy on hydrogen scale, and E_g is bandgap energy.

Plug in numbers from the previous literature:

- For ZnO: $X = 5.79$ eV, $E_g = 3.21$ eV → that gives us CB $= -0.31$ eV and VB $= +2.90$ eV.
- For CeO_2: $X = 5.56$ eV, $E_g = 2.93$ eV → that works out to CB $= -0.41$ eV and VB $= +2.52$ eV.

These results indicate that the CB potentials are more negative than the reduction potential of $O_2/O_2^{\bullet -}$ (−0.33 eV), enabling superoxide radical formation, while the VB potentials are more positive than the oxidation potential of $H_2O/^{\bullet}OH$ (+2.4 eV), allowing hydroxyl radical generation. Therefore, the band structure is thermodynamically favorable for ROS production, consistent with the radical trapping experiments. Combined with the experimental observations, these findings further confirm the operation of *Z*-scheme heterojunction mechanism in CeO_2–ZnO/biochar system (Table 2).

3.2 Adsorption performance

3.2.1 Contact time effect and kinetics.

The adsorption capacity of CeO_2–ZnO/biochar composite toward tetracycline (TC) and methylene blue (MB) was evaluated over time. Fig. 8a and b demonstrate rapid pollutant uptake within the initial 30 minutes (removing ∼65% of adsorbate), followed by progressively slower adsorption approaching equilibrium at 90 minutes, characteristic of typical two-stage adsorption kinetics. The rapid initial adsorption phase (0–30 min) resulted from readily accessible active sites on the composite surface, while the subsequent plateau ($t > 60$ min) indicated saturation of available adsorption sites. Kinetic modeling (Table 3) revealed excellent fit to pseudo-second-order model ($R^2 > 0.99$), strongly suggesting chemisorption as the rate-limiting step through electron sharing/exchange mechanisms. Pseudo-first-order model yielded lower correlation coefficients, imply limited physisorption contribution.[30]

Table 4 Comparative performance of different materials

Material	MB removal (%)	TC removal (%)	Rate constant (min^{-1})
ZnO	62.3	58.9	0.0128
CeO_2	68.5	64.2	0.0156
CeO_2–ZnO	81.7	79.3	0.0224
CeZB	96.5	91.4	0.0312

3.2.2 Adsorption isotherms. The equilibrium adsorption data for both contaminants exhibited optimal correlation with Langmuir isotherm model ($R^2 > 0.98$, Fig. 9a), demonstrating monolayer coverage on homogeneous adsorption sites with uniform energy distribution. At 25 °C, the maximum Langmuir adsorption capacity according to the Langmuir model was 156.3 mg g^{-1} for methylene blue (MB) and 112.8 mg g^{-1} for tetracycline (TC), while the dimensionless separation coefficient (RL < 1) also confirmed so as to the adsorption process occur in a suitable and preferential manner. In contrast, the Freundlich model (Fig. 9b) showed lower correlation coefficients, indicating that multilayer adsorption or surface heterogeneity did not play a major role in this process, which is consistent with the results presented in Table 3.

3.2.3 pH effect. The adsorption performance exhibited strong pH-dependence, with MB removal efficiency increasing from 45% to 92% as pH rose from 3 to 10. This enhancement stems from decreasing electrostatic repulsion between protonated amino groups (MB^+) and progressively deprotonated, negatively-charged adsorbent surface at higher pH. For TC, optimal adsorption occurred around pH 6–7, where electrostatic interactions and hydrogen bonding were most favorable. At extreme pH values, protonation/deprotonation of surface functional groups led to reduced performance (Fig. 10).

3.3 *Performance degradation of photocatalytic*

3.3.1 Comparative performance and synergistic effect. To validate the synergistic effect of CeO_2–ZnO/biochar (CeZB) composite, comparative experiments were conducted using pure CeO_2, pure ZnO, and binary CeO_2–ZnO under identical conditions (Table 4). Photocatalytic degradation efficiencies for methylene blue (MB) after 90 min were: ZnO: 62.3%, CeO_2: 68.5%, CeO_2–ZnO: 81.7% and CeO_2–ZnO/biochar: 96.5% similarly, for tetracycline (TC): ZnO: 58.9%, CeO_2: 64.2%, CeO_2–ZnO: 79.3% and CeZB: 91.4%. The significantly enhanced performance of the ternary composite confirms a strong synergistic effect, arising from: (i) enhanced charge separation from heterojunction formation, (ii) increased adsorption capacity from biochar, and (iii) enhanced electron transport *via* the conductive carbon matrix. These findings clearly demonstrate that the combined system outperforms individual and binary components, validating synergistic adsorption–photocatalysis mechanism.

3.3.2 Degradation efficiency. The CeO_2–ZnO/biochar composite under visible light irradiation, showed superior photocatalytic activity compared to CeO_2, ZnO, and biochar alone. The degradation efficiencies after 90 minutes were 96.5% for MB and 91.4% for TC using the ternary composite, while pure ZnO and CeO_2 achieved only 62.3% and 68.5%, respectively. Biochar alone exhibited negligible photocatalytic activity.

3.3.3 Kinetic studies. According to the Langmuir–Hinshelwood mechanism, photodegradation kinetics followed the pseudo-first-order model (Fig. 8, up). The rate constant (*k*) for MB degradation with the composite was 0.0312 min^{-1}, significantly higher than ZnO (0.0128 min^{-1}) and CeO_2 (0.0156 min^{-1}), confirming the enhanced degradation capability due to synergistic interactions and efficient charge separation.

3.3.4 Reactive species identification. To figure out how the photocatalytic process actually works, we ran some radical scavenging tests using specific quenchers. Isopropanol (IPA) was used to trap benzoquinone (BQ), hydroxyl radicals ($^{\bullet}OH$) for superoxide radicals ($O_2^{\bullet-}$), and EDTA-2Na to capture photogenerated holes (h^+).

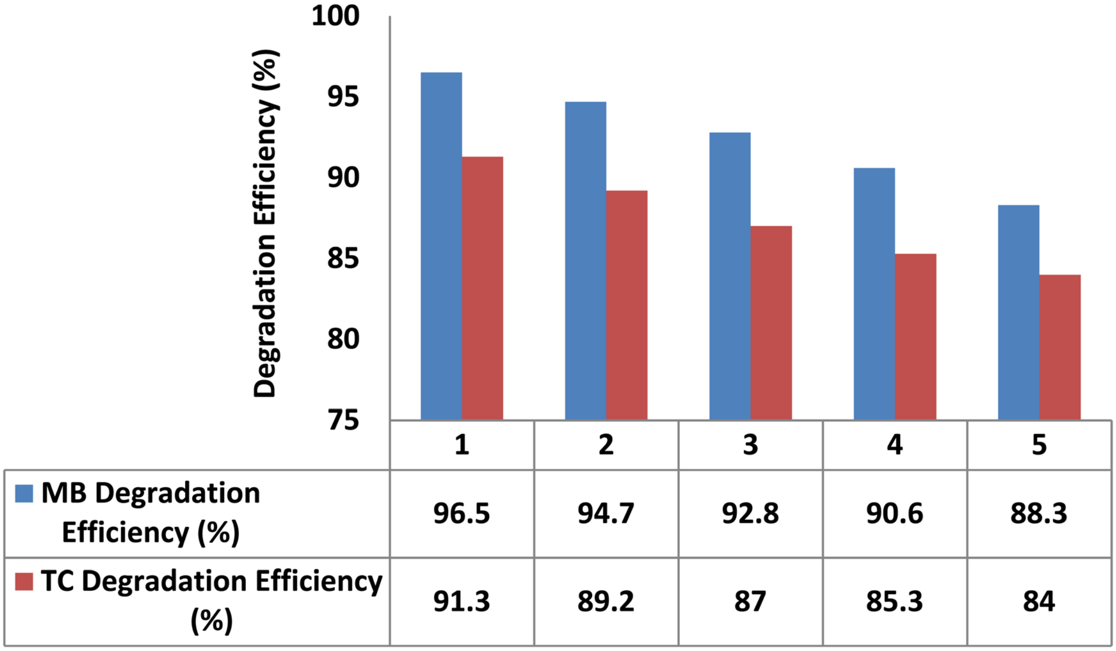

	1	2	3	4	5
🟦 MB Degradation Efficiency (%)	96.5	94.7	92.8	90.6	88.3
🟥 TC Degradation Efficiency (%)	91.3	89.2	87	85.3	84

Fig. 11 Photocatalytic reusability of CeO_2–ZnO/biochar composite over five consecutive cycles.

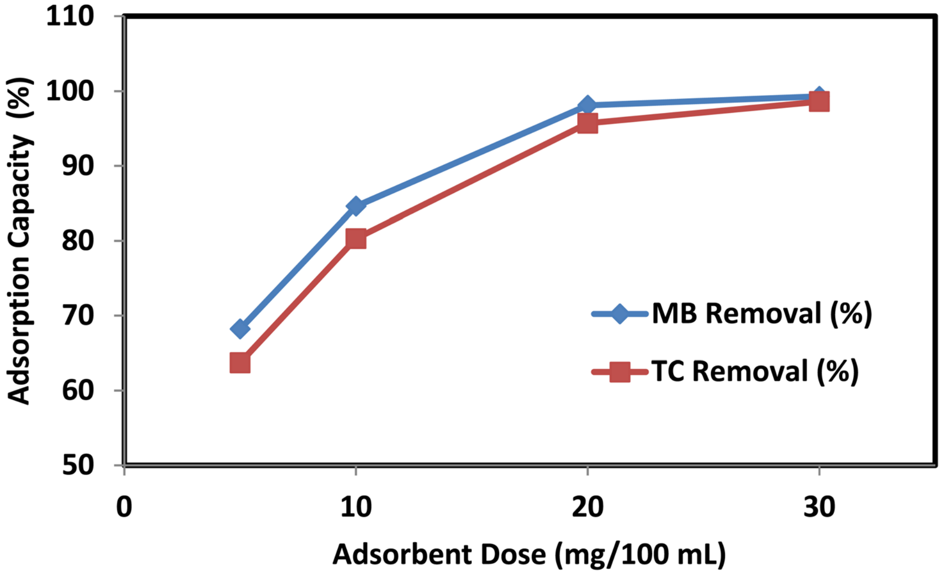

Fig. 12 Adsorbent dosage effect (0.1–1.0 g L^{-1}) on adsorption capacity (%) for MB and TC using the CeO_2–ZnO/biochar composite under conditions: pH 7.0 ± 0.2, $C_0 = 20$ mg L^{-1}, $T = 25$ °C, $t = 90$ min.

Table 5 Adsorbent dosage effect ranging from 0.1 to 1.0 g L^{-1} on equilibrium adsorption capacity (q_e) of MB and TC

Adsorbent dose (mg/100 mL)	MB removal (%)	TC removal (%)	MB q_e (mg g^{-1})	TC q_e (mg g^{-1})
5	68.2	63.7	136.4	127.4
10	84.6	80.3	84.6	80.3
20	98.1	95.7	49.1	47.8
30	99.3	98.6	33.1	32.9

The results are shown in Fig. 8–10, basically the degradation of MB reached 96.5%, however after adding quenchers dropped it is significantly down to about 21% with IPA, around 34% with BQ, and roughly 68% with EDTA-2Na. The big drop with IPA and BQ tells us that $^{\bullet}OH$ and $O_2^{\bullet-}$ are the main players here, while holes only play a supporting role.

These observations line up well with *Z*-scheme charge transfer mechanism. In this setup:

- Electrons from ZnO conduction band turn O_2 into $O_2^{\bullet-}$
- Holes from CeO_2 valence band turn H_2O into $^{\bullet}OH$.

On top of that, biochar helps electrons move around more easily, which boosts the overall generation of reactive oxygen species (ROS).

3.3.5 Reusability and structural stability. Five consecutive photocatalytic cycles were used to assess the CeO_2–ZnO/biochar composite's reusability (Fig. 11). Good durability was demonstrated by the composite's retention of over 88% of its initial activity for MB and 84% for TC. XRD and FTIR analyses were carried out both before and after the fifth cycle to further verify the composite's structural stability. The preservation of the biochar matrix and surface chemistry is indicated by the FTIR spectra and XRD patterns, which show no discernible changes in characteristic functional groups. These findings support the CeO_2–ZnO/biochar composite's suitability for long-term applications by showing that it retains its chemical stability and structural integrity during repeated photocatalytic operations.

3.3.6 Metal ion leaching and stability assessment. To assess the environmental safety and long-term applicability of CeO_2–ZnO/biochar composite, ICP-OES analysis was performed on treated solution after the 5th photocatalytic cycle. The concentrations of leached metal ions were found to be Zn^{2+} (0.012 mg L^{-1}) and Ce ions: (0.006 mg L^{-1}). These values are significantly lower than typical environmental discharge limits, indicating strong structural stability of the composite and minimal risk of secondary contamination. Strong interfacial interactions between CeO_2, ZnO, and the biochar matrix effectively immobilize the metal oxides, resulting in low leaching behavior. These findings confirm that CeO_2–ZnO/biochar composite is a stable and environmentally sustainable material suitable for repeated wastewater treatment applications.

3.4 Effect of adsorbent dose on adsorption performance

The adsorption efficiency and pollutant uptake capacity are significantly influenced by the amount of adsorbent used in the treatment process. Fig. 12 and Table 5 illustrate under optimum conditions, the removal efficiencies for the two model pollutants tetracycline (TC) and methylene blue (MB) increased gradually as the composite dose increased from 5 mg to 30 mg

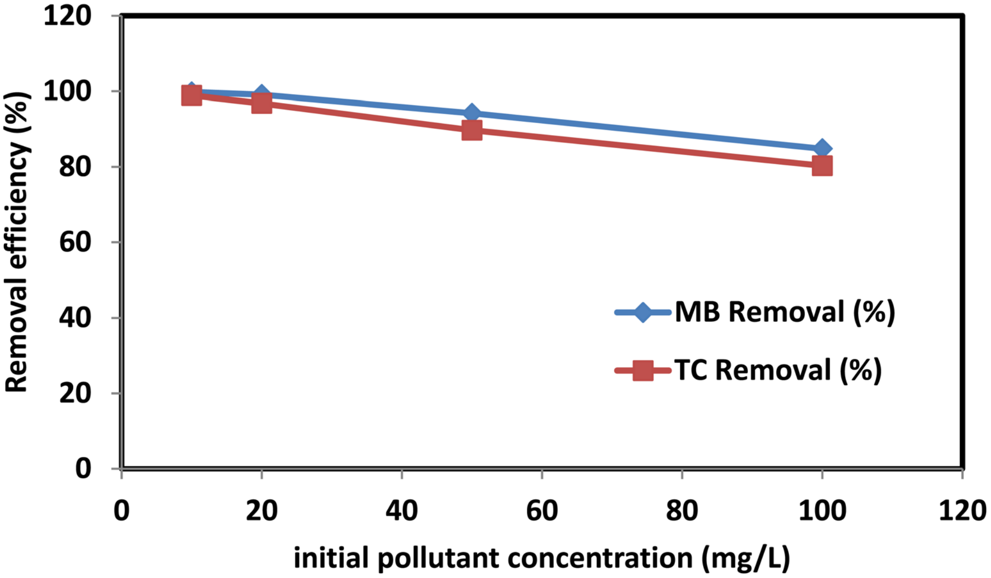

Fig. 13 Effect of initial concentration (10–100 mg L^{-1}) on removal efficiency (%) for MB and TC using the CeO_2–ZnO/biochar composite under conditions: pH 7.0 ± 0.2, $C_0 = 20$ mg L^{-1}, $T = 25$ °C, $t = 90$ min.

Table 6 Initial pollutant concentration effect on removal efficiency and the adsorption capacity

Initial concentration (mg L^{-1})	MB removal (%)	TC removal (%)	MB q_e (mg g^{-1})	TC q_e (mg g^{-1})
10	99.8	98.9	49.9	49.5
20	99.1	96.8	49.6	48.4
50	94.2	89.7	118.0	112.1
100	84.8	80.3	212.0	201.0

per 100 mL. In particular, the efficiency of TC removal increased from 63.7% to 98.6%, while that of MB removal improved from 68.2% to 99.3%. Dosage-dependent increases in (a) functional group availability (–OH, –COOH) and (b) accessible adsorption sites, as verified by site density calculations, are the cause of the observed improvement. This allows for increased interaction with pollutant molecules. The presence of abundant –OH, –COOH, Ce^{3+}, and Zn^{2+} functional sites contributed to both physical and chemical adsorption processes.

However as the adsorbent dose increased, the adsorption capacity per unit mass (q_e, mg g^{-1}) showed an inverse trend. During the same dose range, q_e decreased for TC from 127.4 mg g^{-1} to 32.9 mg g^{-1}, and for MB, it decreased from 136.4 mg g^{-1} at 5 mg dose to 33.1 mg g^{-1} at 30 mg. Commonly known as the "adsorbent dose effect" or "concentration dilution effect," this phenomenon occurs when the number of available pollutant molecules per gram of adsorbent decreases as the dose increase, resulting in underutilization of active sites.[31] Furthermore, because active sites may overlap or cluster when particles aggregate at higher doses, particularly in mesoporous materials like biochar, the effective surface area available for adsorption may be decreased. Overall, these findings point to 20 mg/100 mL as the ideal dosage for obtaining high removal efficiency (>95%) and maintaining an acceptable adsorption capacity (49.1 mg g^{-1} for MB, 47.8 mg g^{-1} for TC). For scalable and economical implementation in real-world wastewater treatment systems, this balance is essential.[32]

3.5 Effect of initial pollutant concentration on adsorption performance

The initial pollutant concentration plays a significant role in adsorption kinetics by modulating both the concentration gradient (driving force for mass transfer) and adsorbent saturation thresholds. According to Fig. 13 and Table 6, the equilibrium adsorption capacity (q_e) increased proportionately (45 to 128 mg g^{-1} for TC, and from 48 to 132 mg g^{-1} for MB), indicating improved site utilization at higher concentrations, whereas the removal efficiency (%) showed an inverse relationship with initial concentration (decreasing from 95% to 72% for MB and 92% to 68% for TC across 10–100 mg L^{-1}). The removal efficiencies were remarkably high, exceeding 96% for both pollutants at lower concentrations (10–20 mg L^{-1}). For example, at 10 mg L^{-1}, TC removal was 98.9% with a q_e of 49.5 mg g^{-1} and MB removal was 99.8% with a q_e of 49.9 mg g^{-1}. Favorable site-to-pollutant stoichiometry, where a large number of surface functional groups (–OH, –COOH) and porous structures enable unhindered access to binding sites, is the cause of this improved low-concentration performance. The removal efficiencies dropped slightly to 84.8% for MB and 80.3% for TC as the concentration increased to 100 mg L^{-1}. On the other

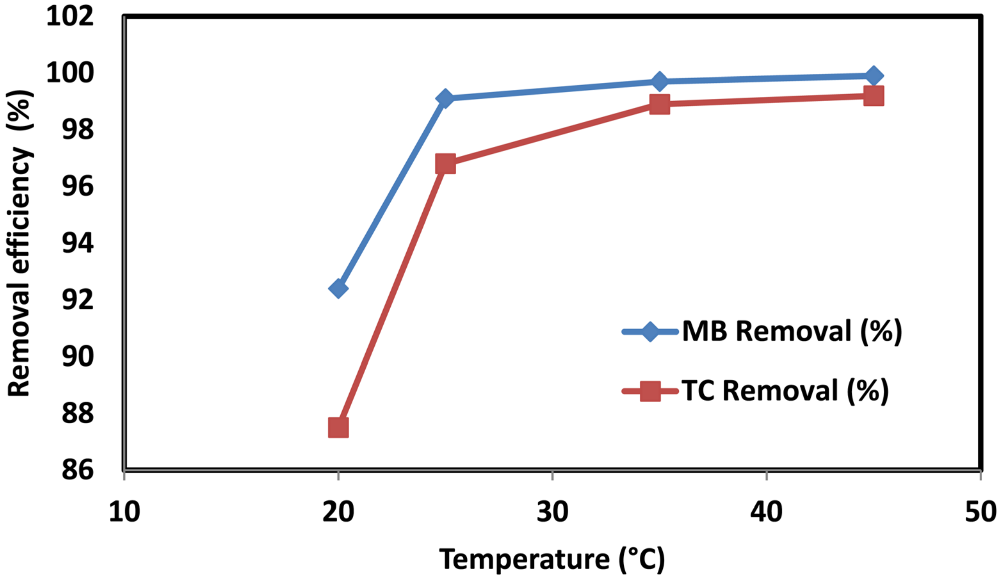

Fig. 14 Effect of temperature on adsorption capacity (q_e) and the removal efficiency of both methylene blue (MB) and tetracycline (TC) using a CeO_2–ZnO composite supported on biochar, (adsorbent dose = 20 mg; initial concentration = 20 mg L^{-1}; pH ≈ 7; contact time = 90 min).

Table 7 Effect of temperature on the adsorption capacity (q_e) of CeO_2–ZnO/biochar composite for pollutants

Temperature (°C)	MB removal (%)	TC removal (%)	MB q_e (mg g^{-1})	TC q_e (mg g^{-1})
20	92.4	87.5	46.2	43.8
25	99.1	96.8	49.6	48.4
35	99.7	98.9	49.8	49.5
45	99.9	99.2	49.9	49.6

hand, the adsorption capacity per gram of adsorbent increased dramatically, reaching 201.0 mg g^{-1} for TC and 212.0 mg g^{-1} for MB, suggesting improved loading onto the composite material. The adsorption isotherm theory, which states that at higher concentrations, the increased pollutant gradient By establishing a steeper concentration gradient between the bulk solution and the adsorbent surface, this process improves mass transfer and speeds up molecular diffusion in accordance with Fick's first law. Even though some active sites start to saturate, the greater number of pollutant molecules increases the probability of collision and interaction with available binding sites, increasing q_e.[32]

The higher capacity at elevated concentrations also reflects the composite's robust adsorption potential and structural compatibility with both dye and antibiotic molecules. This makes the CeO_2–ZnO/biochar system highly suitable for real wastewater treatment, where pollutant concentrations may vary widely.

3.6 Effect of temperature on adsorption performance

By altering the kinetics, equilibrium, and thermodynamics of the adsorbent–adsorbate system, temperature has a major impact on adsorption behavior. The CeO_2–ZnO/biochar composite performed better against methylene blue (MB) and tetracycline (TC) when the temperature was raised from 20 °C to 35 °C, as shown in Fig. 14 and Table 7. With adsorption capacities of 46.2 and 43.8 mg g^{-1}, respectively, removal efficiencies at 20 °C were 92.4 percent (MB) and 87.5 percent (TC). Adsorption significantly improved with temperature, reaching maximum removal efficiencies of 99.7 percent for MB and 98.9 percent for TC at 35 °C, with corresponding adsorption capacities of 49.8 mg g^{-1} (MB) and 49.5 mg g^{-1} (TC).

The trend continued to improve slightly until it reached 45 ° C, where the highest removal efficiency (99.9% for MB and 99.2% for TC) was observed. The q_e values stayed stable at about 49.9 and 49.6 mg g^{-1}, respectively. These findings indicate an endothermic adsorption process, wherein higher temperatures enhance pollutant molecule mobility and reduce solution viscosity, promoting greater diffusion into the composite's porous structure. Higher temperatures may also activate more adsorption sites by making the surface more active and breaking up interactions between solutes and solvents. This makes interactions between absorbates and adsorbents more probable. However, the incremental improvements beyond 35 ° C were marginal, indicating that the system approaches thermodynamic equilibrium. The relatively stable q_e values beyond 35 °C also imply CeZB composite maintains excellent performance at ambient to slightly elevated temperatures, which is advantageous for real-world applications without requiring thermal energy input. These observations are consistent with

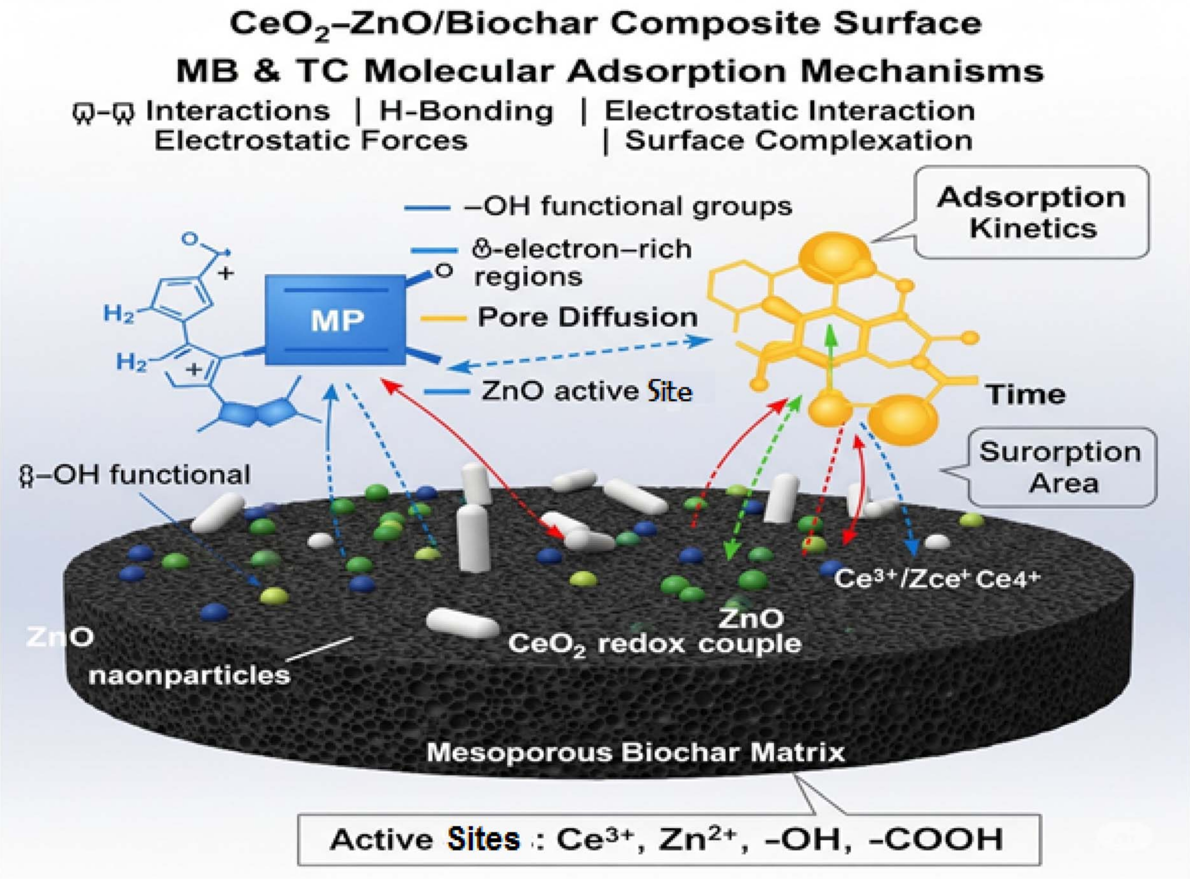

Fig. 15 Schematic illustration of adsorption mechanisms of methylene blue (MB) and tetracycline (TC) on CeO_2–ZnO/biochar ternary composite surface. Key interactions include π–π stacking with biochar, electrostatic attraction (MB), hydrogen bonding (TC), surface complexation with Ce^{3+}/Zn^{2+}, and intraparticle pore diffusion.

prior studies indicating physisorption with possible chemisorption contributions, where the thermodynamic favourability increases slightly with temperature due to endothermic surface interactions.

3.7 Effect of Co-existing ions and natural organic matter

To evaluate the practical applicability of CeO_2–ZnO/biochar composite in real wastewater systems, the effects of common co-existing ions (Cl^-, NO_3^-, CO_3^{2-}) and natural organic matter (NOM, represented by humic acid) were investigated. The presence of Cl^- and NO_3^- showed negligible influence on the degradation efficiency, with removal efficiencies remaining above 90%, indicating minimal competition for active sites or reactive species. In contrast, CO_3^{2-} slightly reduced photocatalytic efficiency (to ~85%), due to its scavenging effect on hydroxyl radicals ($^{\bullet}OH$), forming less reactive carbonate radicals. The presence of NOM (10 mg L^{-1} humic acid) resulted in a moderate decrease in efficiency (~80%), which can be attributed to: Competitive adsorption on active sites, light shielding effect and ROS scavenging behavior. Despite these effects, the composite maintained high removal performance, demonstrating its robustness under realistic water matrix conditions. These results confirm that CeZB composite exhibits strong resistance to interference from co-existing species, highlighting its suitability for real wastewater treatment applications.

3.8 Adsorption mechanism of MB and TC on CeO_2–ZnO/biochar composite

The superior adsorption performance of CeO_2–ZnO/biochar (CeZB) composite toward both methylene blue (MB) and tetracycline (TC) can be attributed to the synergistic effects of multiple adsorption mechanisms operating concurrently at the composite surface. These mechanisms are illustrated in Fig. 15. The biochar matrix plays a pivotal role by offering a high specific surface area (215.3 m^2 g^{-1}) and abundant functional groups as hydroxyl (–OH), carboxyl (–COOH), and aromatic domains, which improve interaction with organic molecules. For both MB and TC, π–π stacking interactions occur between the aromatic rings of the pollutants and the conjugated carbon network of the biochar, facilitating rapid surface binding.[33]

Because MB is cationic, electrostatic interactions are particularly common in this scenario. The surface functional groups bearing negative charges of biochar attract the positively charged MB molecules at neutral pH (~7), increasing the

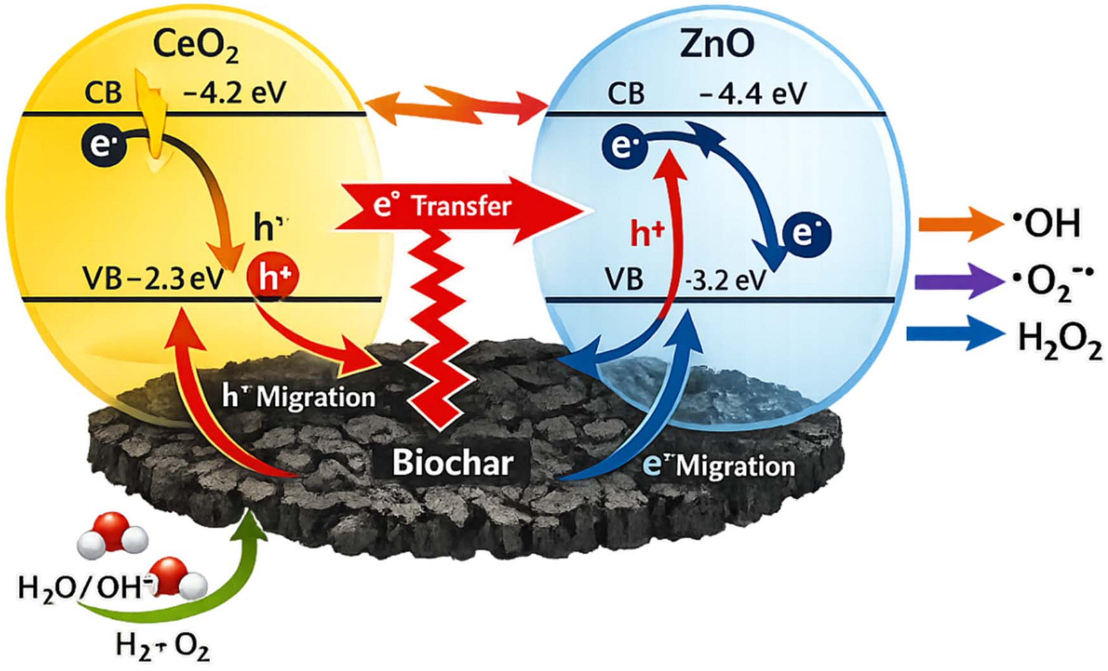

Fig. 16 Schematic illustration of *Z*-scheme charge transfer mechanism in CeO_2–ZnO/biochar composite showing electron–hole migration and ROS generation pathways.

adsorption affinity. Since TC is amphoteric and contains several ionizable groups, adsorption is facilitated by hydrogen bonding with the surface's –OH and –COOH groups. Furthermore, surface complexation mechanisms are probably at involved, especially with TC, which has several donor atoms (–OH, $-NH_2$, –C=O) that can chelate with surface-present Ce^{3+}, Ce^{4+}, or Zn^{2+} ions. According to the observed pseudo-second-order kinetics, this ligand-like interaction facilitates chemisorption.[34–36]

In addition, the porous architecture of the composite, especially from the biochar component (average pore diameter ~8.1 nm), allows for intraparticle diffusion, further enhancing the uptake of pollutant molecules through capillary and diffusion-driven processes. The collective contributions of electrostatic attraction, π–π interactions, hydrogen bonding, surface coordination, and pore diffusion mechanisms are schematically summarized in Fig. 15, providing a comprehensive understanding of the adsorption behavior of CeZB composite.[37]

3.9 Interfacial charge transfer mechanism of CeO_2–ZnO heterojunction

The enhanced photocatalytic performance of the CeO_2–ZnO/biochar composite can only be explained by comprehending the interfacial charge transfer mechanism between CeO_2 and ZnO. The conduction band (CB) and valence band (VB) positions of ZnO and CeO_2 were estimated based on reported electronegativity values and bandgap energies from UV-Vis DRS analysis (Fig. 16). ZnO has a valence band potential of +2.7 eV (*vs.*) and a conduction band potential of about −0.5 eV, whereas CeO_2 shows VB at +2.7 eV and CB at roughly −0.2 eV. Photogenerated electrons would move from ZnO (higher CB) to CeO_2 (lower CB) in a typical Type-II heterojunction, whereas holes would move in the opposite direction. The strong production of reactive oxygen species ($^{\bullet}OH$ and $O_2^{\bullet-}$) seen in the scavenger experiments, however, would be contradicted by this mechanism, which would lower the charge carriers' redox capacity. Rather, photogenerated electrons in the conduction band of CeO_2 recombine with holes in the valence band of ZnO in a direct *Z*-

Table 8 Cost comparison with conventional methods

Treatment method	Material cost (\$ kg^{-1})	Operational cost	Lifespan/reusability
CeO_2–ZnO/biochar	\$200–\$800 (initial)	Moderate (light + regeneration)	High (5+ cycles)
Activated carbon	\$1–\$5 (bulk)	Low (but requires frequent replacement)	Limited (single-use)
TiO_2 photocatalysts	\$50–\$200	High (UV light dependency)	Moderate (3–5 cycles)
Advanced oxidation (AOPs)	High (chemicals + energy)	Very high (H_2O_2, O_3, *etc.*)	Single-use

Table 9 Comparison with reported photocatalysts

Material	Pollutant	Removal (%)	Light source	Reference
TiO_2	MB	65–75	UV	46
ZnO	MB	60–70	UV	47
CeO_2	TC	55–65	Visible	48
ZnO/biochar	MB	80–88	Visible	49
CeO_2–ZnO (binary)	MB	80–85	Visible	50
CeZB (this work)	MB	96.5	Visible	This work
CeZB (this work)	TC	91.4	Visible	This work

scheme mechanism, which is strongly supported by the results. This allows electrons in ZnO CB to reduce O_2 to $O_2^{\bullet-}$ radicals while holes in CeO_2 VB oxidize H_2O to $^{\bullet}OH$ radicals because it maintains the highly reductive electrons in ZnO CB and the strongly oxidative holes in CeO_2 VB. This mechanism is consistent with the results of the scavenger study, which identified superoxide and hydroxyl radicals as dominant species. Furthermore, biochar acts as a conductive bridge that inhibits recombination, further facilitating electron transport.

The marked increase in the photocatalytic activity of the CeO_2–ZnO/Biochar composite can thus be explained by the formation of a *Z*-scheme heterostructure. This type of structure enhances the separation and transport of photo-generated charges with high efficiency, while simultaneously maintaining the system's oxidative and reductive potential, thereby enhancing its reactivity,[19–24] (Fig. 16).

4 Cost analysis and comparative assessment of CeO_2–ZnO/biochar ternary composite

There exists an urgent requirement for sophisticated, affordable treatment methods owing to the increasing contamination of water supplies by persistent organic and inorganic contaminants. CeO_2–ZnO/biochar ternary composite has demonstrated remarkable potential as a dual-purpose material in this regard, fusing photocatalytic degradation activity with synergistic adsorption capacity for thorough pollutant removal. The cost of producing CeO_2–ZnO/biochar composite includes energy-intensive synthesis techniques like hydrothermal/sol–gel processing ($100–$500 per batch) and calcination (~500–800 °C), as well as raw materials like biochar ($50–$200 per ton), CeO_2 ($50–$100 kg^{-1}), and ZnO ($2–$5 kg^{-1}). The total estimated cost at the lab level is $200–$800 kg^{-1}. However, through process optimization and bulk procurement, production scaling could result in cost savings of 30–50%. The composite's high adsorption capacity reduces the need for replacements, and its photocatalytic reusability (80–90% efficiency after 5 cycles) increases cost-effectiveness. Long-term operating costs are still influenced by the energy used for UV/visible light activation, which ranges from $0.10 to $0.50 kWh^{-1}. All things considered, when optimized for large-scale applications, the composite offers a sustainable and financially feasible wastewater treatment solution.[38–45]

4.1 Comparative assessment of performance

With a large surface area (300–800 m^2 g^{-1}) from the biochar, CeO_2–ZnO/biochar composite exhibits superior adsorption efficiency (Table 8). This allows for approximately 90% removal of heavy metals and dyes, compared to the capacity of zeolites/clay (~50–70%) and activated carbon (limited to non-degradative adsorption). By utilizing ZnO's UV activity and CeO_2's oxygen vacancies, the composite achieves >90% pollutant removal (MB, RhB, and phenol) under visible light during photocatalytic degradation. This greatly outperforms ZnO nanoparticles, which are unstable and resistant to photo corrosion, and pure TiO_2 (~60% efficiency, UV-dependent). Compared to traditional materials, the ternary composite is a highly effective and sustainable wastewater treatment solution because of its dual functionality (adsorption + photocatalysis) and visible-light responsiveness.

4.2 Comparison with reported photocatalysts

The CeO_2–ZnO/biochar composite was evaluated against previously reported photocatalysts for organic pollutant removal (Table 9). The results indicate that the developed material exhibits enhanced adsorption capacity and higher photocatalytic efficiency under visible light irradiation compared with conventional photocatalysts such as TiO_2, ZnO, and several binary composite systems, highlighting its improved overall performance.

For instance, TiO_2-based systems typically achieve removal efficiencies of 60–75% under UV light, while ZnO-based systems suffer from rapid charge recombination and photo corrosion. In contrast, CeZB composite achieved >96% degradation of MB and >91% degradation of TC under visible light, highlighting its enhanced performance. The improved efficiency is attributed to *Z*-scheme heterojunction formation, oxygen vacancies in CeO_2, the high adsorption capacity of biochar, and the resulting enhancement in charge separation and ROS generation. These results position CeO_2–ZnO/biochar composite as a highly competitive and advanced material for wastewater treatment applications.

5 Conclusions

The hydrothermal method was successfully used to create a new CeO_2–ZnO/Biochar (CeZB) composite, which was then evaluated for its ability to simultaneously adsorb and photocatalytically degrade tetracycline (TC) and methylene blue (MB). The composite showed a narrowed bandgap of 2.48 eV, improved light absorption in the visible spectrum, and a high specific surface area of 215.3 m^2 g^{-1}. With adsorption capacities of 198.6 mg g^{-1} for MB and 163.2 mg g^{-1} for TC, as well as photocatalytic degradation efficiencies exceeding 96 percent and 91 percent, respectively, under visible light, the CeZB composite also showed exceptional performance. The adsorption mechanism was described through equilibrium and kinetic studies. The process follows a pseudo-second-order model, according to the kinetic results, suggesting that chemical interactions primarily regulate the adsorption rate. The equilibrium data fit the Langmuir model well, indicating that adsorption takes place on the material's surface as a uniform monolayer with a single molecule occupying each adsorption site. Additionally, mechanistic investigations, such as energy band analysis and free radical scavenging experiments, have demonstrated that the development of a *Z*-scheme heterostructure between CeO_2 and ZnO, bolstered by the function of a highly conductive biochar matrix, is responsible for the increase in photocatalytic activity. More effective charge separation and the production of reactive oxygen species (ROS) were also facilitated by the presence of oxygen voids and the coexistence of mixed Ce^{3+}/Ce^{4+} oxidation states. The ternary composite outperformed binary and single-component systems in terms of performance, and experimental comparisons showed a definite synergistic effect. Furthermore, the composite demonstrated excellent stability, with virtually no metal leaching and only a minor drop in efficiency after five operating cycles, confirming its environmental safety and potential for effective reuse. Its applicability in actual wastewater systems is further highlighted by its resistance to interference from co-existing ions and natural organic matter. Practically speaking, CeZB composite presents a viable, affordable, and sustainable way to handle complicated wastewater that contains a variety of pollutants. Scaling up the synthesis process, evaluating long-term performance in continuous flow systems, and investigating the removal of a broader range of emerging pollutants are some future research directions.

Author contributions

The research tasks were divided as follows: Mahmoud F. Mubarak oversaw the formal analyses, developed the research methodology, organized and analyzed the data, and contributed to securing resources and utilizing software. Elbadawy A. Kamoun was responsible for project management, resource procurement, and drafting the initial manuscript. M. Y. Nassar, Elbadawy A. Kamoun, and Tahany Mahmoud participated in preparing the initial draft of the article, providing scientific oversight, and utilizing software, in addition to reviewing and refining the revised version of the manuscript. All authors approved the current final version of the manuscript and agreed to submit it for publication.

Conflicts of interest

The authors declare that they have no known competing financial interests or personal relationships that could have appeared to influence the work reported in this paper.

Data availability

The datasets used and/or analyzed during the current study are available from the corresponding authors on reasonable request.

Acknowledgements

This work was supported and funded by the Deanship of Scientific Research, Vice Presidency for Graduate Studies and Scientific Research, King Faisal University (KFU), Saudi Arabia [Project No. KFU261625]. Authors used DeepSeek AI software during the preparation of this work to improve language, readability, and grammar of specific sections. After using this tool, authors reviewed and edited the content as needed and take full responsibility for the content of published manuscript.

References

1 Z. Liu, F. Zhang, C. Li and C. Inoue, Enhanced visible light response and characterization of nanoscale TiO_2/WO_{3-x} composite photocatalyst by sol–gel synthesis, *Catal. Lett.*, 2022, 1–14, DOI: 10.1007/s10562-022-04079-z.

2 J. Q. Xiao, N. V. Mdlovu, K. S. Lin, C. J. Chang and Z. W. Chen, Degradation of rhodamine B under visible-light with nanotubular Ag@AgCl@ AgI photocatalysts, *Catal. Today*, 2020, **358**, 155–163.

3 H. Widiyandari, I. Firdaus, V. G. S. Kadarisman and A. Purwanto, Optical properties and photocatalytic activities of tungsten oxide (WO_3) with platinum co-catalyst addition, *AIP Conf. Proc.*, 2016, **1712**, 050027, DOI: 10.1063/1.4941910.

4 S. Madihi-Bidgoli, S. Asadnezhad, A. Yaghoot-Nezhad and A. Hassani, Azurobine degradation using Fe_2O_3@ multi-walled carbon nanotube activated peroxymono sulfate (PMS) under UVA-LED irradiation: performance, mechanism and environmental application, *J. Environ. Chem. Eng.*, 2021, **9**, 106660, DOI: 10.1016/j.jece.2021.106660.

5 D. Toloman, M. Stefan, O. Pana, A. M. Rostas, T. D. Silipas, F. Pogacean, S. Pruneanu, C. Leostean, L. Barbu-Tudoran and A. Popa, Transition metal ions as a tool for controlling the photocatalytic activity of MWCNT-TiO_2 nanocomposites, *J. Alloys Compd.*, 2022, **921**, 166095, DOI: 10.1016/j.jallcom.2022.166095.

6 A. Hassani, M. Faraji and P. Eghbali, Facile fabrication of mpg-C3N4/Ag/ZnO nanowires/Zn photocatalyst plates for photodegradation of dye pollutant, *J. Photochem. Photobiol., A*, 2020, **400**, 112665, DOI: 10.1016/j.jphotochem.2020.112665.

7 V. D. Binas, K. Sambani, T. Maggos, A. Katsanaki and G. Kiriakidis, Synthesis and photocatalytic activity of Mn-doped TiO_2 nanostructured powders under UV and visible light, *Appl. Catal., B*, 2012, **113–114**, 79–86.

8 C. B. Anucha, I. Altin, E. Bacaksiz and V. N. Stathopoulos, Titanium dioxide (TiO_2)-based photocatalyst materials activity enhancement for contaminants of emerging concern (CECs) degradation: in the light of modification strategies, *Chem. Eng. J. Adv.*, 2022, **10**, 100262, DOI: 10.1016/j.ceja.2022.100262.

9 X. X. Chen, Y. P. Li, X. Y. Pan, D. Cortie, X. T. Huang and Z. G. Yi, Photocatalytic oxidation of methane over silver decorated zinc oxide nano catalysts, *Nat. Commun.*, 2016, 7, 12273.

10 Q. Tao, X. Huang, J. Bi, R. Wei, C. Xie, Y. Zhou, L. Yu, H. Hao and J. Wang, Aerobic Oil-Phase Cyclic Magnetic Adsorption to Synthesize 1D Fe_2O_3@TiO_2 Nanotube Composites for

Enhanced Visible-Light Photocatalytic Degradation, *Nanomaterials*, 2020, **10**, 1345.

11 T. Montini, M. Melchionna, M. Monai and P. Fornasiero, Fundamentals and Catalytic Applications of CeO_2-Based Materials, *Chem. Rev.*, 2016, **116**, 5987–6041.

12 A. D. Liyanage, S. D. Perera, K. Tan, Y. Chabal and K. J. Balkus, Synthesis, Characterization, and Photocatalytic Activity of Y-doped CeO_2 nanorods, *ACS Catal.*, 2014, **4**, 577–584.

13 M. A. Subhan, N. Uddin, P. Sarker, A. K. Azad and K. Begum, Photoluminescence, photocatalytic and antibacterial activities of $CeO_2\cdot CuO\cdot ZnO$ nanocomposite fabricated by co-precipitation method, *Spectrochim. Acta A Mol. Biomol. Spectrosc.*, 2015, **149**, 839–850.

14 Z. S. Shi, Q. Q. Tan and D. F. Wu, Enhanced CO_2 hydrogenation to methanol over TiO_2 nanotubes-supported CuO-ZnO-CeO_2 catalyst, *Appl. Catal., A*, 2019, **581**, 58–66.

15 S. Patnaik, G. Swaina and K. M. Parida, Highly efficient charge transfer through a double Z-scheme mechanism by a Cu-promoted MoO_3/g-C_3N_4 hybrid nanocomposite with superior electrochemical and photocatalytic performance, *Nanoscale*, 2018, **10**, 5950–5964.

16 S. Issarapanacheewin, K. Wetchakun, S. Phanichphant, W. Kangwansupamonkon and N. Wetchakun, A novel CeO_2/Bi_2WO_6 composite with highly enhanced photocatalytic activity, *Mater. Lett.*, 2015, **156**, 28–31.

17 T. F. Jiang, T. F. Xie, Y. Zhang, L. P. Chen, L. L. Peng, H. Y. Li and D. J. Wang, Photoinduced charge transfer in ZnO/Cu_2O heterostructure films studied by surface photovoltage technique, *Phys. Chem. Chem. Phys.*, 2010, **12**, 15476–15481.

18 N. Wetchakun, S. Chaiwichain, B. Inceesungvorn, K. Pingmuang, S. Phanichphant, A. I. Minett and J. Chen, $BiVO_4$/CeO_2 Nanocomposites with High Visible-Light-Induced Photocatalytic Activity, *ACS Appl. Mater. Interfaces*, 2012, **4**, 3718–3723.

19 W. Li, X. Li, X. Xiao, *et al.*, A Multimodal Sensory Textile Using Programmable Ferroelectric Nanocomposites, *Adv. Mater.*, 2025, **37**(43), e07169.

20 Q. Bautista, J. Rigual, J. Lloreda, A. Fons, J. Nogués, E. Gómez, B. Sepúlveda and A. Serrà, Synergistic photothermal/photocatalytic activation of peroxymonosulfate using SrFe12O19@Ni-P core@shell microparticles for energy efficient water remediation, *Chem. Eng. J.*, 2026, **530**, 173570.

21 W. Li, G. Xie, X. Huo, L. Que, H. Tai, Y. Jianga and Y. Su, Piezoelectric composites for gas sensing: evolution of sensing and transduction designs, *J. Mater. Chem. C*, 2025, **13**, 13582–13606.

22 X. Luo, Bo Liu, W. Li, B. Li, H. Yuan and Y. Su, Triple-enhanced sensory textiles for self-powered infrared detection, *Nano Energy*, 2025, **145**, 111438.

23 P. Cai, B. Li, Y. Zhan, X. Feng, X. Pu, L. Wang, Z. Chen, Z. Liu and S. Bi, Re4+/Te4+ Co-doped Cs2ZrCl6 double perovskite microcrystals: Broadening excitation range and boosting luminescent performance for near-infrared lighting and non-destructive quality inspection, *Mater. Today Chem.*, 2025, **48**, 102954.

24 Li Yi, Z. Zhang, H. Zhu, J. Sun, M. Guo, Xi Zeng, Y. Li and M. Hashimoto, Plasticized PVC/CNT flexible electrodes for highly responsive, stable, and durable soft actuators and wearable sensors, *Sens. Actuators, B*, 2026, **447**(1), 138894.

25 A. El-Denglawey, M. F. Mubarak and H. &Selim, Tertiary Nanocomposites of Meta kaolinite/Fe_3O_4/SBA-15 Nanocomposite for the Heavy Metal Adsorption: Isotherm and Kinetic Study, *Arab. J. Sci. Eng.*, 2022, **47**, 455–476.

26 W. Plazinski, J. Dziuba and W. &Rudzinski, Modeling of sorption kinetics: the pseudo-second order equation and the sorbateintraparticle diffusivity, *Adsorption*, 2013, **19**, 1055–1064.

27 E. D. Revellame, D. L. Fortela, W. Sharp, R. Hernandez and M. E. Zappi, Adsorption kinetic modeling using pseudo-first order and pseudo-second order rate laws: A review, *Clean. Eng. Techn.*, 2020, **1**, 100032.

28 M. Vigdorowitsch, A. Pchelintsev, L. Tsygankova and E. Tanygina, Freundlich Isotherm: An Adsorption Model Complete Framework, *Appl. Sci.*, 2021, **11**(17), 8078.

29 H. A. El-Sabban, M. F. Mubarak and M. A. Diab, PPy-NTs/C/TiO_2/poly(ether sulfone) porous composite membrane: Efficient ultrafiltration of Evans blue dye from industrial wastewater, *Synth. Met.*, 2023, **297**, 117383.

30 E. Torrik, M. Soleimani and M. T. &Ravanchi, Application of Kinetic Models for Heavy Metal Adsorption in the Single and Multicomponent Adsorption System, *Int. J. Environ. Res.*, 2019, **13**, 813–828.

31 J. López-Luna, L. E. Ramírez-Montes, S. Martinez-Vargas, *et al.*, Linear and nonlinear kinetic and isotherm adsorption models for arsenic removal by manganese ferrite nanoparticles, *SN Appl. Sci.*, 2019, **1**, 950.

32 M. F. Mubarak, T. A. Yousef, S. A. Salim, M. Khairy, E. A. Kamoun and T. Mahmoud, Meta-kaolinite metal oxide quaternary composite for layered double hydroxide applied to a new frontier in adsorption technology: Synthesis, adsorption performance and kinetics study, *Inorg. Chem. Commun.*, 2025, **178**(2), 114647.

33 S. S. Imam, R. Adnan and N. H. Mohd Kaus, The photocatalytic potential of BiOBr for wastewater treatment: a mini-review, *J. Environ. Chem. Eng.*, 2021, **9**, 105404, DOI: 10.1016/j.jece.2021.105404.

34 P. N. T. Ho, T. B. Nguyen, C. P. Huang, R. an Doong, C. W. Chen and C. Di Dong, In-situ immobilization of Ag/AgCl on sulfurized g-C3N4 nanosheet for enhancing visiblelight driven photocatalysis toward simultaneous oxidation of tetracycline and reduction of Cr(VI) in water, *J. Environ. Chem. Eng.*, 2023, **11**, 109453, DOI: 10.1016/j.jece.2023.109453.

35 R. Wang, Y. Wang, S. Mao, X. Hao, X. Duan and Y. Wen, Different morphology MoS2 Over the g-C3N4 as a boosted photo-catalyst for pollutant removal under visiblelight, *J. Inorg. Organomet. Polym. Mater.*, 2021, **31**, 32–42, DOI: 10.1007/s10904-020-01626-2.

36 J. Li, G. Yu, L. Pan, C. Li, F. You, S. Xie, Y. Wang, J. Ma and X. Shang, Study of ciprofloxacin removal by biochar obtained from used tea leaves, *J. Environ. Sci.*, 2018, **73**, 20–30, DOI: 10.1016/j.jes.2017.12.024.

37 M. Ahmaruzzaman, Biochar based nanocomposites for photocatalytic degradation of emerging organic pollutants from water and wastewater, *Mater. Res. Bull.*, 2021, **140**, 111262, DOI: 10.1016/j.materresbull.2021.111262.

38 T. G. Ambaye, M. Vaccari, E. D. van Hullebusch, A. Amrane and S. Rtimi, Mechanisms and adsorption capacities of biochar for the removal of organic and inorganic pollutants from industrial wastewater, *Int. J. Environ. Sci. Technol.*, 2021, **18**, 3273–3294, DOI: 10.1007/s13762-020-03060-w.

39 M. F. Arkaan, R. F. Ekaputri, I. Fatimah and A. Kamari, Physicochemical and photocatalytic activity of hematite/biochar nanocomposite prepared from salacca skin waste, *Sustain. Chem. Pharm.*, 2020, **16**, 100261, DOI: 10.1016/j.scp.2020.100261.

40 X. Cai, J. Li, Y. Liu, Z. Yan, X. Tan, S. Liu, G. Zeng, Y. Gu, X. Hu and L. Jiang, Titanium dioxide-coated biochar composites as adsorptive and photocatalytic degradation materials for the removal of aqueous organic pollutants, *J. Chem. Technol. Biotechnol.*, 2018, **93**, 783–791, DOI: 10.1002/jctb.5428.

41 M. Chen, C. Bao, D. Hu, X. Jin and Q. Huang, Facile and low-cost fabrication of ZnO/biochar nanocomposites from jute fibers for efficient and stable photodegradation of methylene blue dye, *J. Anal. Appl. Pyrolysis*, 2019, **139**, 319–332, DOI: 10.1016/j.jaap.2019.03.009.

42 J. Fito, K. K. Kefeni and T. T. I. Nkambule, The potential of biochar-photocatalytic nanocomposites for removal of organic micropollutants from wastewater, *Sci. Total Environ.*, 2022, **829**, 154648, DOI: 10.1016/j.scitotenv.2022.154648.

43 M. F. Mubarak, T. A. Yousef, S. A. Salim, M. Khairy, E. A. Kamoun and T. Mahmoud, Meta-kaolinite metal oxide quaternary composite for layered double hydroxide applied to a new frontier in adsorption technology: Synthesis, adsorption performance and kinetics study, *Inorg. Chem. Commun.*, 2025, **178**(2), 114647.

44 M. F. Mubarak, T. A. Yousef, S. A. Salim, M. M. Abou-Krisha, E. A. Kamoun and T. Mahmoud, Design and functionalization of a hierarchical Cu-BTC/Zeolite A4 composite with tannic acid for high-performance heavy metal removal: Synergistic adsorption mechanisms, kinetic insights, and reusability evaluation, *Appl. Mater. Today*, 2026, **49**, 103123.

45 A. S. Morshedy, E. A. Kamoun, M. Y. Nassar, A. S. El-Khouly, T. Mahmoud and M. F. Mubarak, *ChemPlusChem*, 2026, **91**, e202500740.

46 M. M. Khan, S. F. Adil and A. Al-Mayouf, Metal oxides as photocatalysts, *J. Saudi Chem. Soc.*, 2015, **19**(5), 462–464.

47 K. M. Lee, C. W. Lai, K. S. Ngai and J. C. Juan, Recent developments of zinc oxide based photocatalyst in water treatment technology: A review, *Water Res.*, 2016, **88**, 428–448.

48 C. Lai, F. Xu, M. Zhang, B. Li, S. Liu, H. Yi and H. Yang, Facile synthesis of CeO2/carbonate doped Bi2O2CO3 Z-scheme heterojunction for improved visible-light photocatalytic performance, *J. Colloid Interface Sci.*, 2021, **588**, 283–294.

49 Z. Salehi and S. Jafari, Different morphologies of zinc oxide deposited on biochar support for enhanced visible light photocatalytic degradation of methylene blue, *J. Water Environ. Nanotechnol.*, 2025, **10**(1), 45–58.

50 M. Abushad, S. Arshad, M. Arshad, H. Ahmed, Riyaz, S. Husain and W. Khan, Structural investigation and improved visible light-driven photocatalytic performance of ZnO/CeO_2 nanocomposites, *J. Mol. Struct.*, 2025, **1333**, 141697.